Angewandte Chemie
Eine Zeitschrift der Gesellschaft Deutscher Chemiker

Supporting Information

Plasma-Induced Nanocrystalline Domain Engineering and Surface Passivation in Mesoporous Chalcogenide Semiconductor Thin Films

A. Ashok, A. Vasanth, T. Nagaura, M. Eguchi, N. Motta, H.-P. Phan, N.-T. Nguyen, J. G. Shapter*, J. Na*, Y. Yamauchi**

Supporting Information

Plasma Induced Nanocrystalline Domain Engineering and Surface Passivation in Mesoporous Chalcogenide Semiconductor Thin Films

Aditya Ashok,[a,b] Arya Vasanth,[c] Tomota Nagaura,[a] Miharu Eguchi,[a,e] Nunzio Motta,[d] Hoang-Phuong Phan,*[a,b] Nam-Trung Nguyen,[b] Joseph G. Shapter,[a] Jongbeom Na,*[a,f] Yusuke Yamauchi*[a,e]

[a] Australian Institute for Bioengineering and Nanotechnology (AIBN), The University of Queensland, Brisbane, Queensland 4072, Australia

[b] Queensland Micro- and Nanotechnology Centre, Griffith University, Brisbane, Queensland 4111, Australia

[c] Amrita Center for Nanosciences and Molecular Medicine, Amrita Vishwa Vidyapeetham, Kochi, Kerala, 682041, India

[d] School of Chemistry and Physics, Queensland University of Technology (QUT), 2 George Street, Brisbane, Queensland 4001, Australia

[e] JST-ERATO Yamauchi Material Space-Tectonics Project and International Center for Materials Nanoarchitectonics (WPI-MANA) National Institute for Materials Science, 1-1 Namiki, Tsukuba, Ibaraki 305-0044, Japan

[f] Research and Development (R&D) Division, Green Energy Institute, Mokpo, Jeollanamdo 58656, Republic of Korea

*Corresponding author. Email: h.phan@griffith.edu.au; j.na@gei.re.kr; y.yamauchi@uq.edu.au

Materials and Methods

Materials

All chemicals and solvents were purchased from Sigma Aldrich (USA) and were not further purified, unless specified otherwise. Copper sulfate (anhydrous $CuSO_4$, ≥99.99%), tellurium dioxide (TeO_2, ≥99%), nitric acid solution (HNO_3, 70%), and tetrahydrofuran (THF, C_4H_8O, ≥99.9%). The di-block copolymers (BCP) of polystyrene-*b*-poly(ethylene oxide) (PS-*b*-PEO) with molecular weights of PS(5,000)-*b*-PEO(2,000), PS(10,000)-*b*-PEO(4,100), and PS(18,000)-*b*-PEO(7,500) were obtained from Polymer Source (Canada). The average molecular weights of the PS and PEO blocks are shown in numbers. All solutions were prepared using double-distilled deionized water (DIW) from a Milli-Q reference water purification system (≥18.2 MΩ·cm).

Preparation of copper telluride (CuTe) electrolyte

Self-assembled micelles, also referred to as BCPs, consist of a hydrophobic PS chain linked to a hydrophilic PEO chain. The electrolyte solution for deposition was prepared with and without BCP to obtain porous and nonporous CuTe films, respectively. BCPs of varying molecular weights were separately dissolved in THF at a fixed ratio of 10 mg in 1 mL, followed by mixing in a 3 M HNO_3 solution at a 1:3 volume ratio under slow stirring conditions. BCPs with different molecular weights, namely, PS(5,000)-*b*-PEO(2,000) as BCP-1, PS(10,000)-*b*-PEO(4,100) as BCP-2, and PS(18,000)-*b*-PEO(7,500) as BCP-3, were used to prepare various pore sizes. When aqueous HNO_3 solution was introduced to the mixture consisting of PS-*b*-PEO dissolved in THF, the hydrophobic PS chain wrapped inward as a core, leaving behind the hydrophilic PEO chain as a shell, resulting in the self-assembly of micelles.

Separately, 80 mM Cu precursor solution (prepared with $CuSO_4$) in DIW and 80 mM Te precursor solution (prepared with TeO_2) in 3 M HNO_3 solution were prepared as stock solutions for Cu and Te. Under the typical conditions, the added volumes of 80 mM Cu precursor solution and 80 mM Te precursor solution were 0.35 and 0.65 mL, respectively. Metal precursor solutions were introduced into the BCP micelle solution and attached to the shell, covering the micelles *via* hydrogen bonds. By changing the amount of Cu and Te precursor solutions, it was possible to control the resulting compositions. In addition, a nonporous (NP) film was prepared without BCP to understand the effect of the micelles.

Electrochemical deposition of CuTe films

Mesoporous and nonporous CuTe films were deposited on gold-coated Si wafers. The electrochemical (EC) deposition was performed with an electrochemical workstation (CH Instruments, CHI 660E, USA) using a single-compartment cell with three-electrode configuration including a working electrode (Au-coated Si wafer of 0.3 cm × 1.5 cm dimension), a counter electrode (Pt gauzes), and a reference electrode (Ag/AgCl in saturated KCl). The electrolytes were then transferred to the electrochemical (EC) cell. When in contact with the electrolyte, the working electrode resulted in successive deposition in an ice bath maintained at approximately 5 °C. The optimal deposition conditions, such as the deposition potentials and precursor concentrations, were

carefully selected, as discussed later. The as-prepared films were immersed in THF at 45 °C to remove the micelles, rinsed in distilled water, and blow-dried in a stream of nitrogen gas (N_2).

Post-treatment on CuTe films

To understand the effect of post-annealing as a part of changing the surface states and improving the domain size, a set of NP, BCP-1, BCP-2, and BCP-3 films were subjected to thermal annealing for a fixed duration of 60 min at a ramp rate of 3 °C min^{-1} at temperatures of 70, 140, and 210 °C under 0.5 Torr pressure. The films were then brought back to room temperature naturally, while maintaining the vacuum pressure. The plasma treatment on thin films was performed using a PlasmaPro 80 (Oxford Instruments, UK) reactive ion etching (RIE) system, operated at a radio frequency (RF) of 13.56 MHz under Ar environment. The opposite electrode was completely masked, ensuring that only the films were exposed to different plasma powers (10, 30, and 50 W). Ar (99.5% purity) was used as the process gas. The exposure times at different plasma powers were controlled during the study.

Characterization

Spectrophotometric analysis of the thin films was performed using a UV-vis spectrophotometer (Shimadzu UV-2600) with an integrating sphere. The films were observed in a spectral window of 300–850 nm by subtracting the Au-coated Si substrate as the background. A slow scan with a sampling interval and slit width of 1 nm was preferred to obtain a better signal-to-noise ratio from the CuTe films with a thickness of a few nanometers. An X-ray diffractometer (Rigaku SmartLab) was used to conduct out-of-plane grazing incidence X-ray diffraction (GIXD) analysis of the thin film samples with Cu Kα radiation at 45 kV and 200 mA. The GIXD scan was collected with a thin film sample thickness between 150 and 400 nm, at a fixed grazing incidence angle of 0.36° and 2θ varying between 10° and 80°. The samples were analyzed under ambient conditions. Finally, the acquired results were processed using EVA, and the PDF-4 databank was used to identify the patterns. X-ray photoelectron spectroscopy (XPS) measurements were performed using a Kratos Axis Ultra XPS instrument with a monochromatic Al Kα source (1486.69 eV) to investigate the elemental composition and chemical state of the material by probing the sample surface at a depth of approximately 10 nm. Survey and high-resolution core-level spectra were recorded at pass energies of 160 and 20 eV, respectively. The binding energy scale for all core-level spectra was charge-corrected by shifting the spectra to 285 eV such that the core-level of C 1s was aligned with respect to the Kratos library. Ultraviolet photoelectron spectroscopy (UPS) analysis was performed using a Kratos Axis supra, with He(I) energy sourced at 21.22 eV and calibrated to 0 eV using standard Au foil. The post-processing of the XPS and UPS spectra was performed using CasaXPS. The architecture of the samples was characterized using a field-emission scanning electron microscope (FE-SEM, JEOL JSM-7001F) with an accelerating voltage of 15 kV. The energy dispersive X-ray (EDX) analysis of the samples was performed to determine the chemical composition of the deposited films. Cross-sectional transmission electron microscopy (TEM) and scanning transmission electron microscopy (STEM) analyses of the samples were performed on an aberration-corrected TEM/STEM (Hitachi HF5000) equipped with an FE electron gun sourced at 200 kV and a symmetrically opposed dual 100 mm^2 Oxford X-Max detector for

EDX, along with high-angle annular dark-field (HAADF) and bright-field (BF) detectors. TEM lamellae of the nonporous and mesoporous samples were prepared using a focused ion beam (FIB) system (FEI Scios). The observable area was secured between ~1 μm thick Pt layers to minimize the damage by Ga ions during the milling process. The lamella was finally polished at low power and then secured onto a Si grid. The analysis was further facilitated using crystallographic tools to understand the crystallographic projections observed through TEM/STEM. Kelvin probe force microscopy (KPFM) and PeakForce tunneling atomic force microscopy (PF-TUNA) were conducted using a Bruker Dimension ICON XR atomic force microscope (AFM) staged in a vibration-free isolation chamber under ambient conditions. For both scans, the samples were prepared by mounting them onto a steel disk with conductive silver paint to ensure electrical continuity from the sample surface to the grounded chuck. This enables a closed electrical system between the grounded sample and cantilever tip under bias. The scans were carried out using a SCM-PIT-V2 cantilever (Bruker), which was made of antimony (n) doped Si and was coated with platinum-iridium on both sides. The conductive tip radius was 15 nm with a 3.0 N m^{-1} spring constant. No additional surface treatment was performed on the samples prior to the scan. The topography and TUNA current were observed in the PF-TUNA tapping mode and then shifted to the KPFM mode to record the contact potential difference (CPD) of the same samples. The scans were performed at a scan rate of 0.7 Hz with 512 points per line. The cantilever was hovered with the PF amplitude maintained at 70 nm. The TUNA current of the samples was profiled under an applied DC bias between 0 to 1.3 V, to extract the effect of charging at the sample surface. Unless specified otherwise, all profiles were acquired for a 1 μm × 1 μm area under ambient conditions. Post-processing of the acquired data was performed using NanoScope Analysis (Bruker). Photoelectrochemical responses of the CuTe films were measured using an electrochemical workstation (CHI 660E) on pristine samples and samples after plasma treatment under AM1.5G illumination (Pico, G2V Optics). The light source was calibrated using a single-crystalline silicon standard, operated at 87 mW cm^{-2} of illumination intensity observed at a fixed focal point. The response was measured using a three-electrode system in a 0.5 M NaOH solution. The transient behavior of the CuTe film was measured by chopping the irradiance in periodic intervals of 20 s on and off cycles. The active area of CuTe was fixed to 0.21 cm^2 for all samples. The samples were irradiated only after the current stabilized (after 500 s) from the linear sweep voltammetry (LSV). Measurements of all the samples were studied at an initial voltage of 0.2 V.

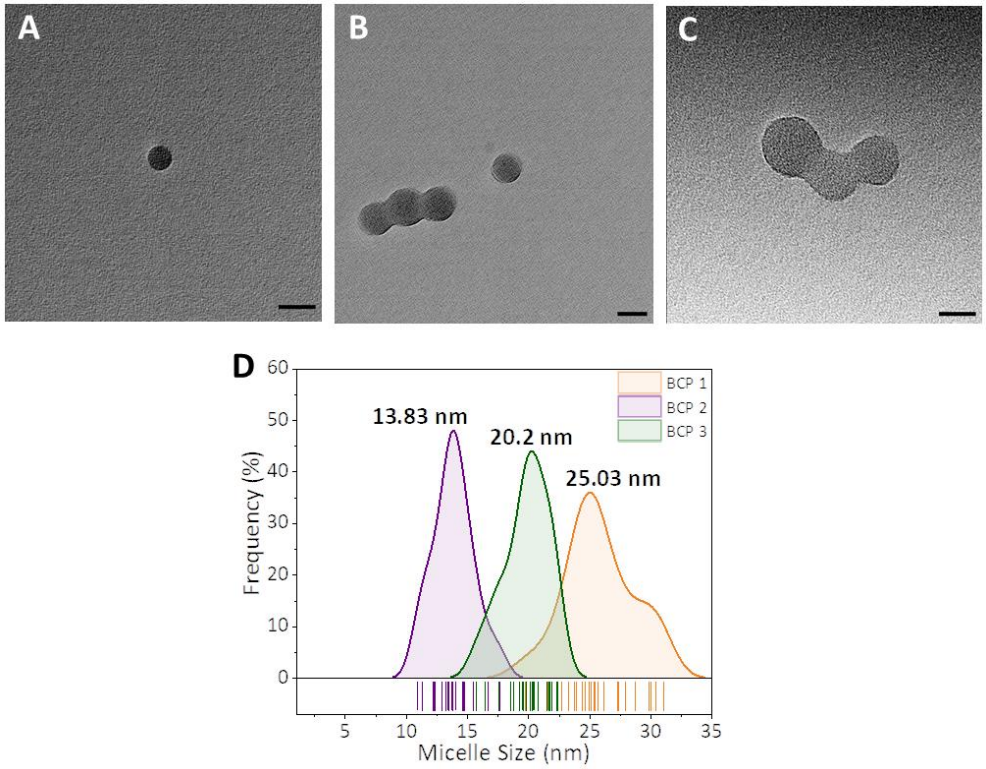

Figure S1. TEM images and size distribution of amphiphilic block co-polymer of different molecular weights. (A) PS(5,000)-*b*-PEO(2,000) as BCP-1, (B) PS(10,000)-*b*-PEO(4,100) as BCP-2, and (C) PS(18,000)-*b*-PEO(7,500) as BCP-3. Scale bar = 20 nm. (D) Micelle size distribution.

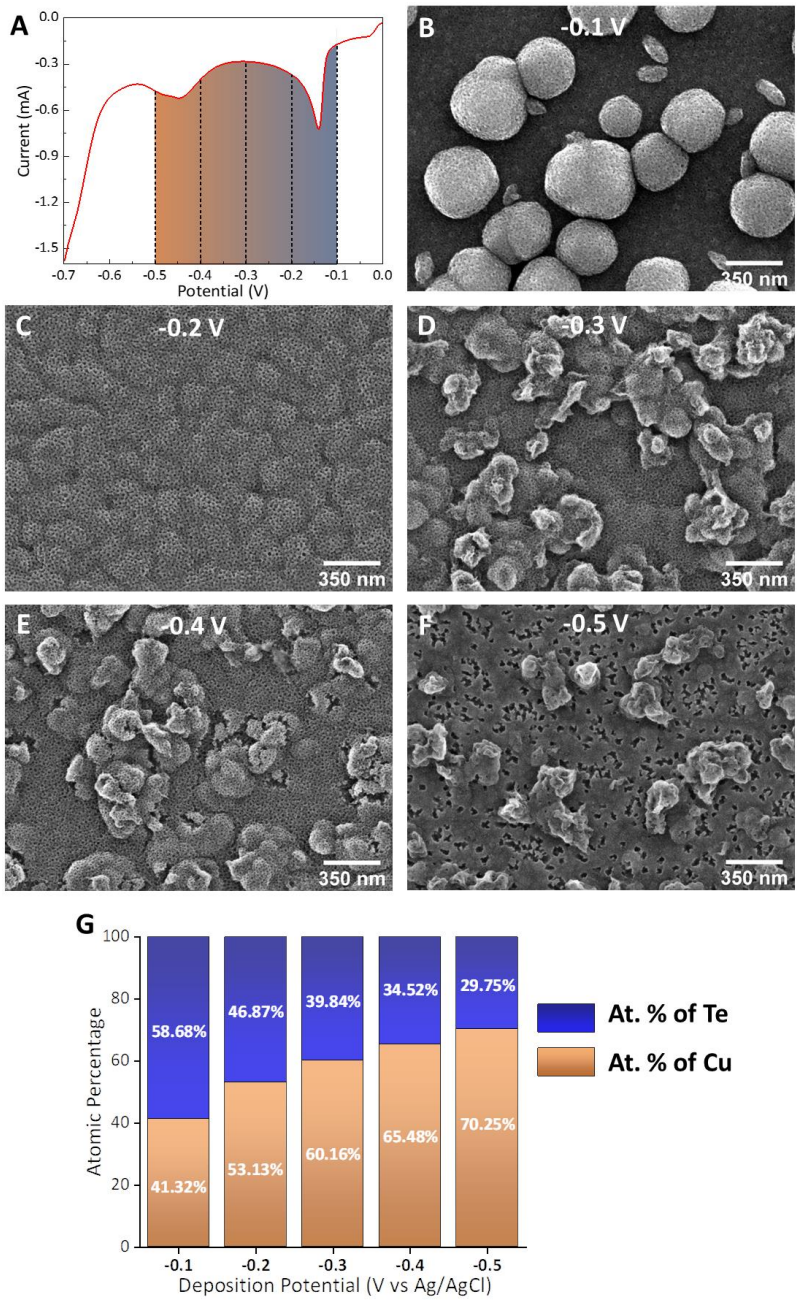

Figure S2. Effect of deposition potential on CuTe. (A) LSV curve at scan rate 10 mV s^{-1} in the electrolyte solution for mesoporous CuTe film. Top-view FE-SEM images of samples deposited at (B) -0.1, (C) -0.2, (D) -0.3, (E) -0.4, and (F) -0.5 V deposition potential for 500 s. (G) Cu and Te concentrations obtained by EDX at respective deposition potentials. The used electrolytes containing PS(18,000)-*b*-PEO(7,500) micelles were prepared by mixing 0.40 mL of 80 mM Cu precursor solution and 0.60 mL of 80 mM Te precursor solution.

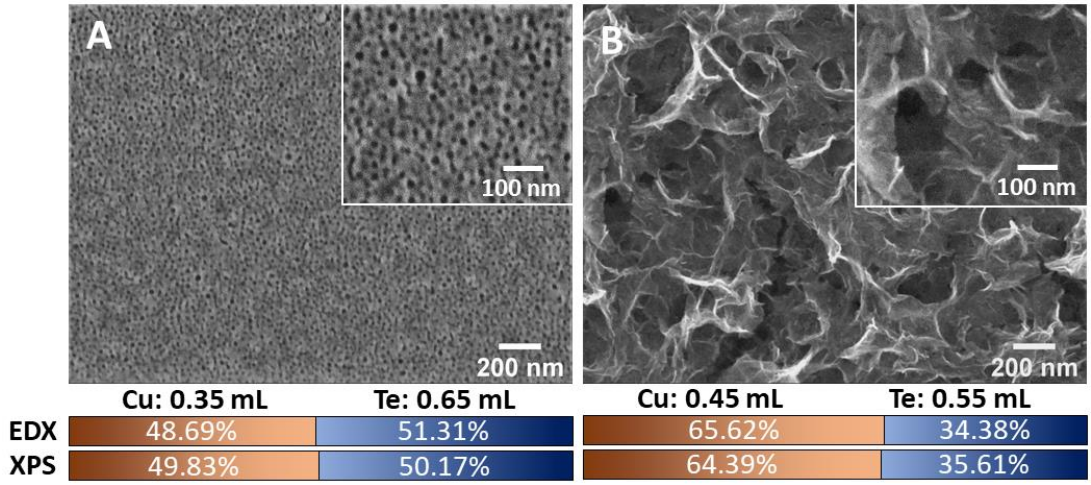

Figure S3. Effect of varying Cu and Te concentrations in electrolyte solution. Top-view FE-SEM images of varying stoichiometry for (A) CuTe and (B) Cu_2Te with corresponding metal precursor volumes to final elemental concentrations in the film (inset: magnified images of each stoichiometry, respectively). The used electrolytes containing PS(18,000)-*b*-PEO(7,500) micelles were prepared by mixing 0.35 mL of 80 mM Cu precursor solution and 0.65 mL of 80 mM Te precursor solution. The applied potential was -0.2 V (*vs*. Ag/AgCl).

Supporting Information Note 1

LSV analysis

Electrolyte solutions with and without micelles were prepared to assess the reduction potentials of Cu and Te using LSV to obtain suitable electrochemical potentials. This optimization experiment was performed using PS(18,000)-*b*-PEO(7,100) micelles in the electrolyte containing 0.4 mL of 80 mM Cu precursor solution and 0.6 mL of 80 mM Te precursor solution. A suitable negative potential initiates the reduction reaction of the metal precursors around the micelles in the electrolyte, resulting in the growth of Cu and Te on the working electrodes with the desired stoichiometry and morphology. Because the work functions of Cu (4.7 eV) and Te (4.95 eV) are fairly similar,[1] the necessary potential for film growth is likewise comparable: -0.03 and -0.14 V (*vs*. Ag/AgCl), respectively. As shown in Figure S2A, a potential range of -0.1 to -0.5 V was selected from the LSV curve. Then, thin films were deposited at selected potentials for 500 s in an ice bath, and the resultant films were characterized by FE-SEM and EDX, as shown in Figures S2B–F and Figure S2G. The thin films obtained at lower deposition potentials (between -0.3 and -0.5 V) showed a significant change in the surface morphology accompanied by a change in the composition, gradually leading to poor pore distribution, as shown in Figures S2D–F. This was due to the rapid aggregation of the metal precursors, mainly Cu. Similarly, at a higher deposition potential, as shown in Figure S2B (-0.1 V), no complete reduction of the metal ions occurred, resulting in the formation of islands. At a deposition potential of -0.2 V, the surface morphology was comparatively flat with a homogeneous pore distribution. A subtle difference in the compositional ratios of Cu : Te was obtained from Figure S2G, depending on the applied potentials. Higher negative deposition potentials resulted in excess deposition of Cu, resulting in a change in the elemental composition and surface morphology. It should be noted that the Cu and Te compositional ratios and concentrations were different between Figures 2 and S2G even the same potential of -0.2 V was applied, because the added volumes of Cu and Te precursor solutions in the starting electrolytes were different (80 mM Cu precursor solution : 80 mM Te precursor solution = 0.4 mL : 0.6 mL in Figure S2G and 0.35 mL : 0.65 mL in Figure 2).

By fixing -0.2 V as the optimal potential, the compositions of the resulting films can be further tuned by altering the initial concentrations of metal precursors in the electrolyte. As shown in Figure S3, the compositional ratio of mesoporous CuTe approached the ideal stoichiometric ratio (1:1) by tuning the concentration of the metal (Cu and Te) precursors. Reproducibility was also greatly improved. In this case, 0.35 mL of 80 mM Cu precursor solution and 0.65 mL of 80 mM Te precursor solution were added to the starting electrolyte. The data in Figure 2 show mesoporous CuTe samples prepared under the same conditions. Furthermore, when the concentrations of the metal (Cu and Te) precursors were drastically changed, mesoporous CuTe and mesoporous Cu_2Te with different crystal structures were successfully prepared. The stoichiometry of the resultant films was examined by EDX and XPS, as displayed below the respective SEM images. The resulting mesoporous CuTe films showed relatively lower surface roughness compared to Cu_2Te with randomly oriented layered structures. At a higher concentration of Cu (~65 at.%) and Te (~35 at.%), the film enters into the Cu_2Te phase (2D material), rearranging

on growth to form the hexagonal crystal structure. This 2D material, when deposited with micelles, resulted in exfoliated or flaky morphology. Therefore, flaky morphology was observed when the Cu content was high.

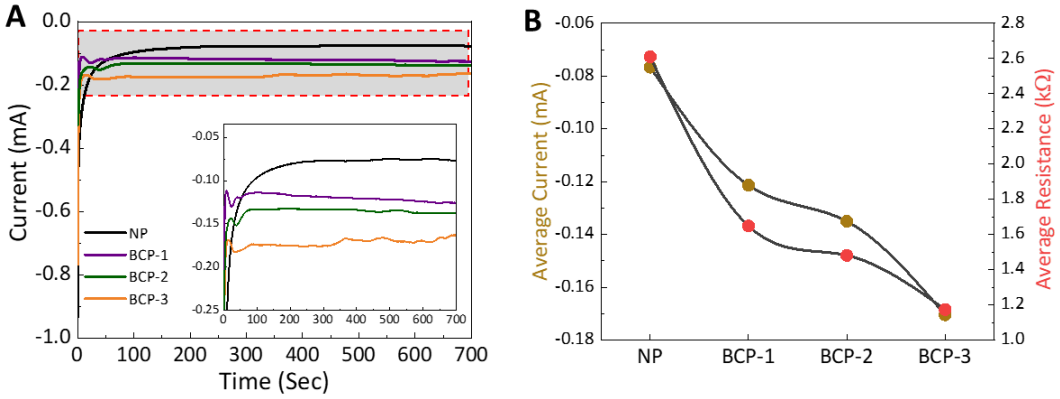

Figure S4. Amperometric *i-t* curves. (A) Currents during deposition of CuTe films at -0.2 V (*vs*. Ag/AgCl). (B) Average currents and corresponding resistance plots upon increasing pore diameters (micelle sizes).

Supporting Information Note 2

Amperometric *i-t* curves

Amperometric currents over time (*i-t*) for depositing the CuTe films were recorded using an electrochemical workstation, as shown in Figure S4. The films were deposited on a conductive substrate (Au), maintaining the deposition potential at -0.2 V (*vs*. Ag/AgCl). This fixed potential was kept constant for the NP and mesoporous films with three different PS-*b*-PEO molecular weights. Under the applied deposition potential, a significant drop in the deposition current was initially observed in all the samples. The NP film deposited in the absence of micelles exhibited a relatively low deposition current, followed by BCP-1, BCP-2, and BCP-3 films (with micelles of increasing molecular weights). This led to a preliminary understanding that the electrochemical deposition (ECD) at -0.2 V produced no significant fluctuations in current observed after 200 s for NP film deposition. In contrast, in the case of mesoporous films, the current fluctuation duration was reduced to only 50 s (Figure S4A). As a result, a flat film morphology can be achieved even at the nanoscale, as confirmed by the SEM images (Figures S2B–D and F–H).

As the deposition progressed on the Au substrate, the resistance of the film increased. This was mainly due to the short-range ordered or random arrangements of atoms in the framework (*i.e.*, polycrystalline CuTe structure), which impede the currents flowing through the framework of the CuTe film (*i.e.*, the observed currents largely decreased after an initial significant drop). However, when the size of the micelles used in the electrolyte increased (Figure S4A), the film resistance gradually decreased (Figure S4B). The observed currents for the mesoporous films were much higher than those of the NP film.

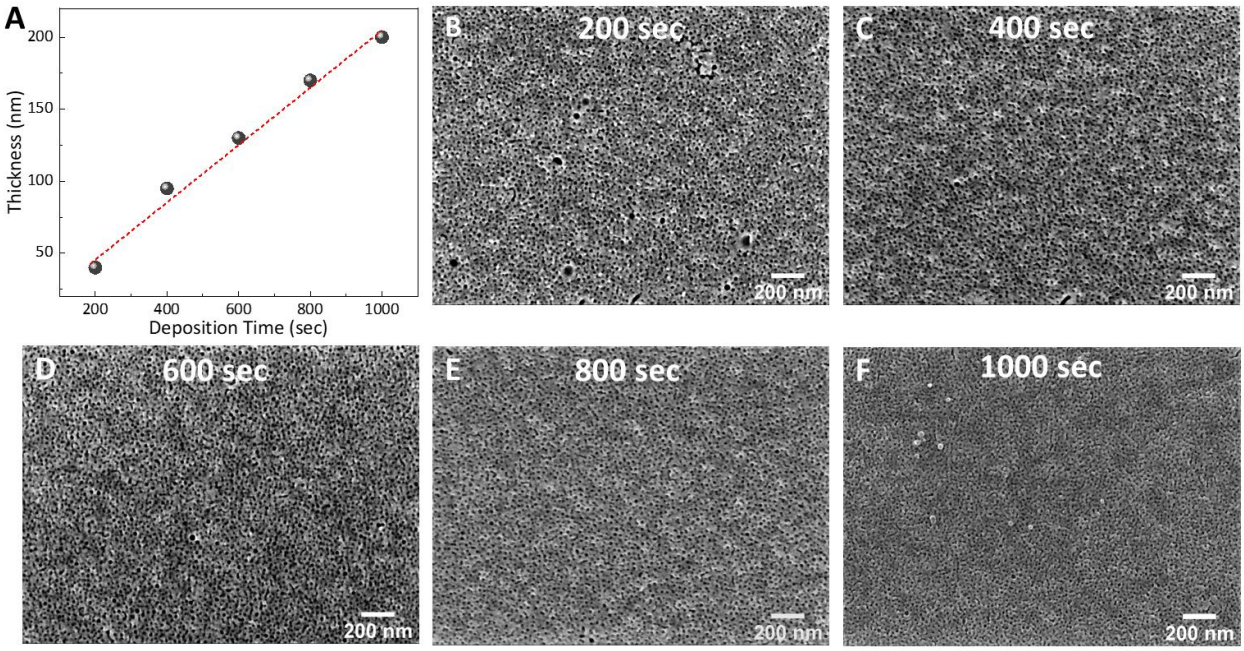

Figure S5. Change in morphology and thickness over time. (A) Film thickness over deposition time (with optimized deposition conditions for BCP-3 films). Top-view FE-SEM images of samples after (B) 200 s, (C) 400 s, (D) 600 s, (E) 800 s, and (F) 1000 s of deposition, respectively.

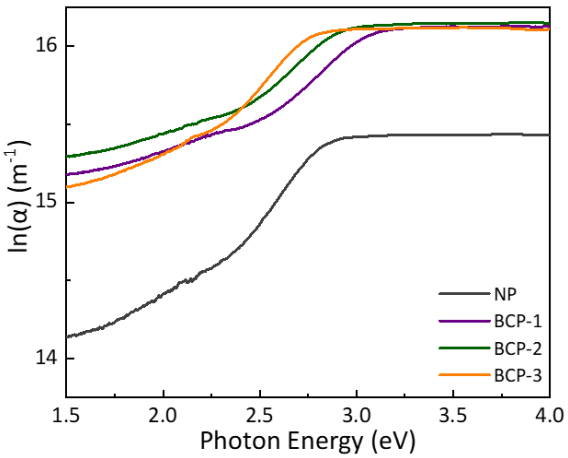

Figure S6. Absorption coefficient *vs*. photon energy of pristine films to examine the Urbach energy.

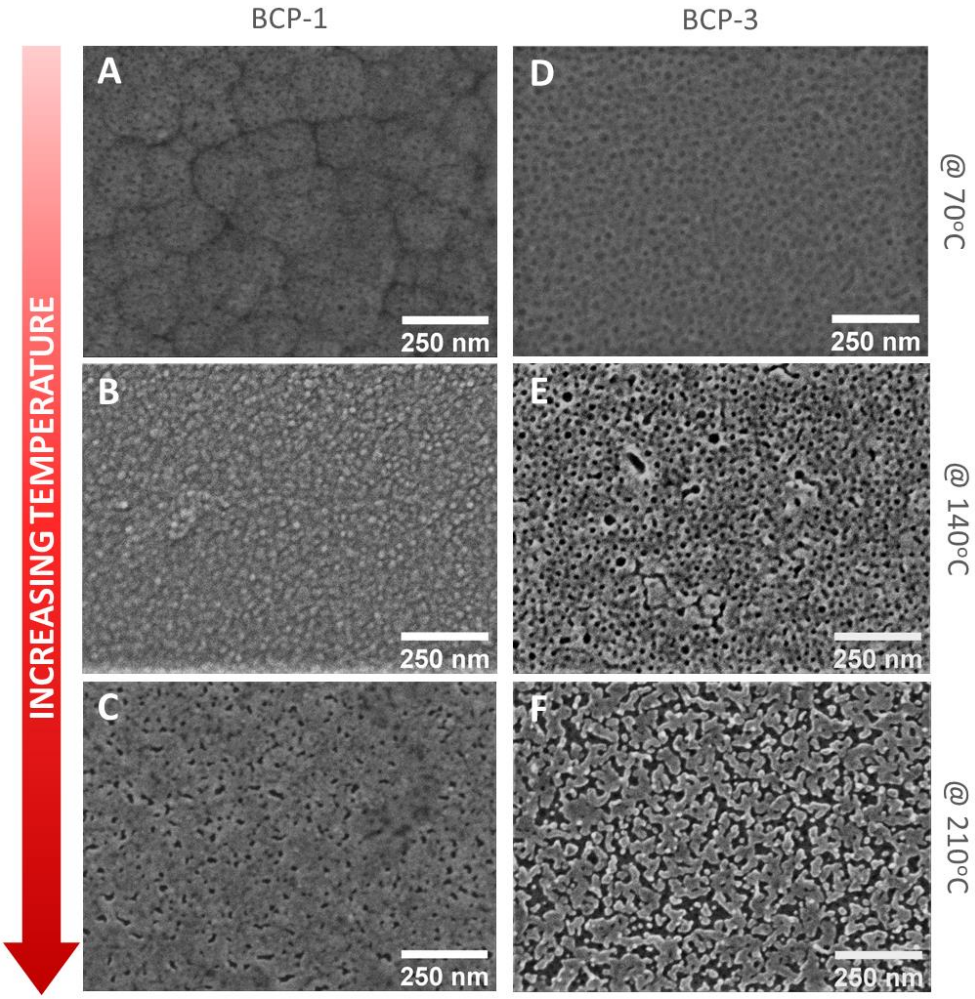

Figure S7. Effect of post-annealing on the morphology of CuTe films. Top-view FE-SEM images of (A-C) small pore BCP-1 film and (D-F) large pore BCP-3 film subjected to post-annealing at (A, D) 70 °C, (B, E) 140 °C, and (C, F) 210 °C.

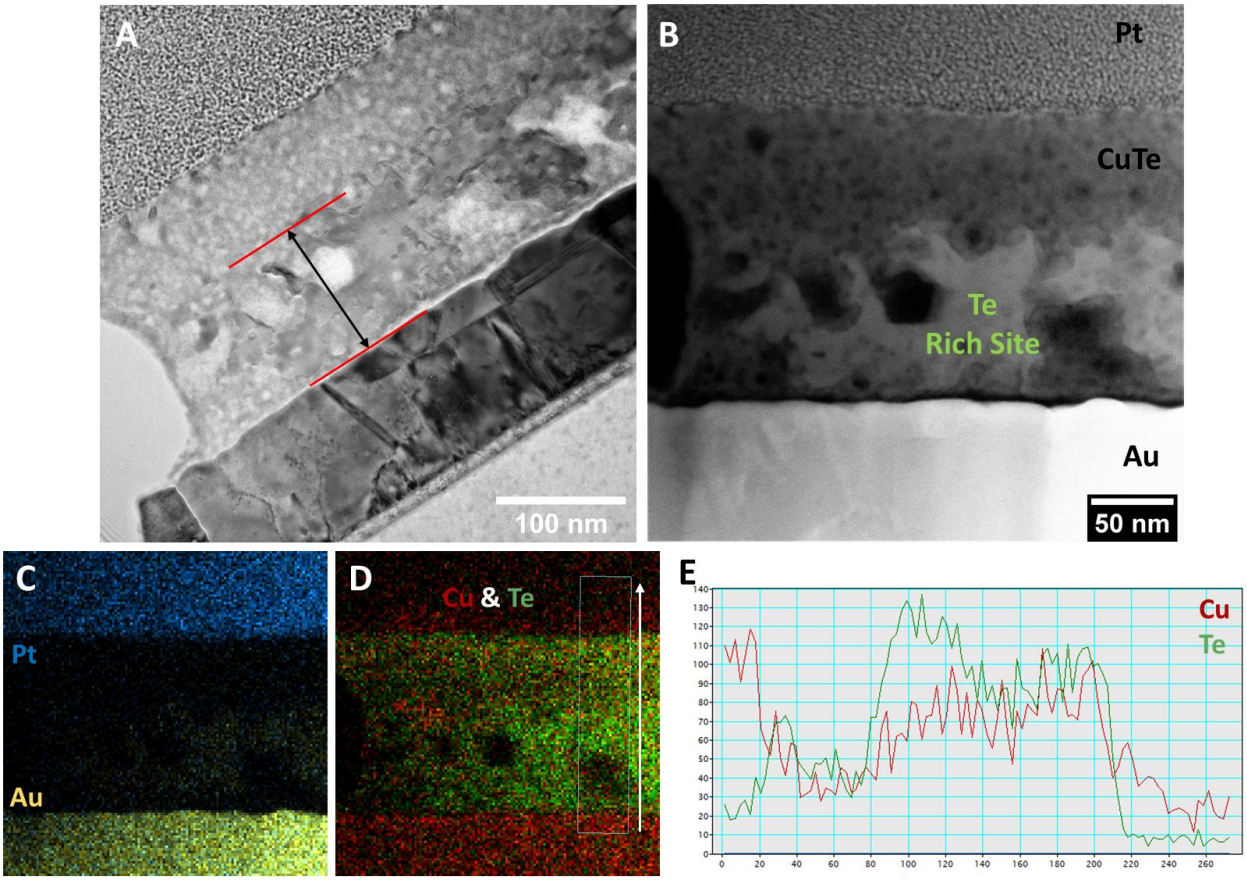

Figure S8. STEM images and EDX on the thermally treated films. (A) Cross-sectional TEM image of BCP-1 film and (B) its corresponding HAADF image after thermal annealing at 140 °C, showing collapsed pore structures. EDX of (C) Pt and Au layer, (D) Cu and Te representing migration of Cu and aggregation of Te, and (E) line profile, directed along the white arrow in (D).

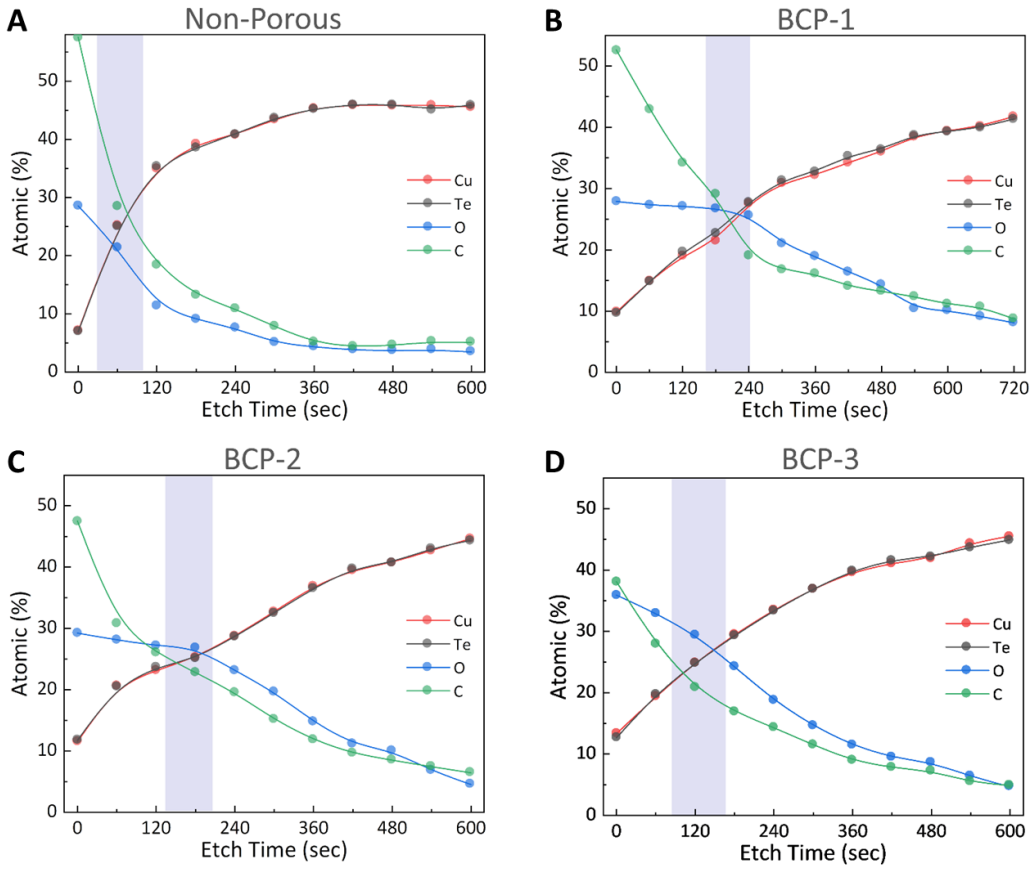

Figure S9. Atomic percentage of elements extracted at different etch cycles from XPS depth profile of (A) NP film and (B-D) mesoporous films with different pore diameters.

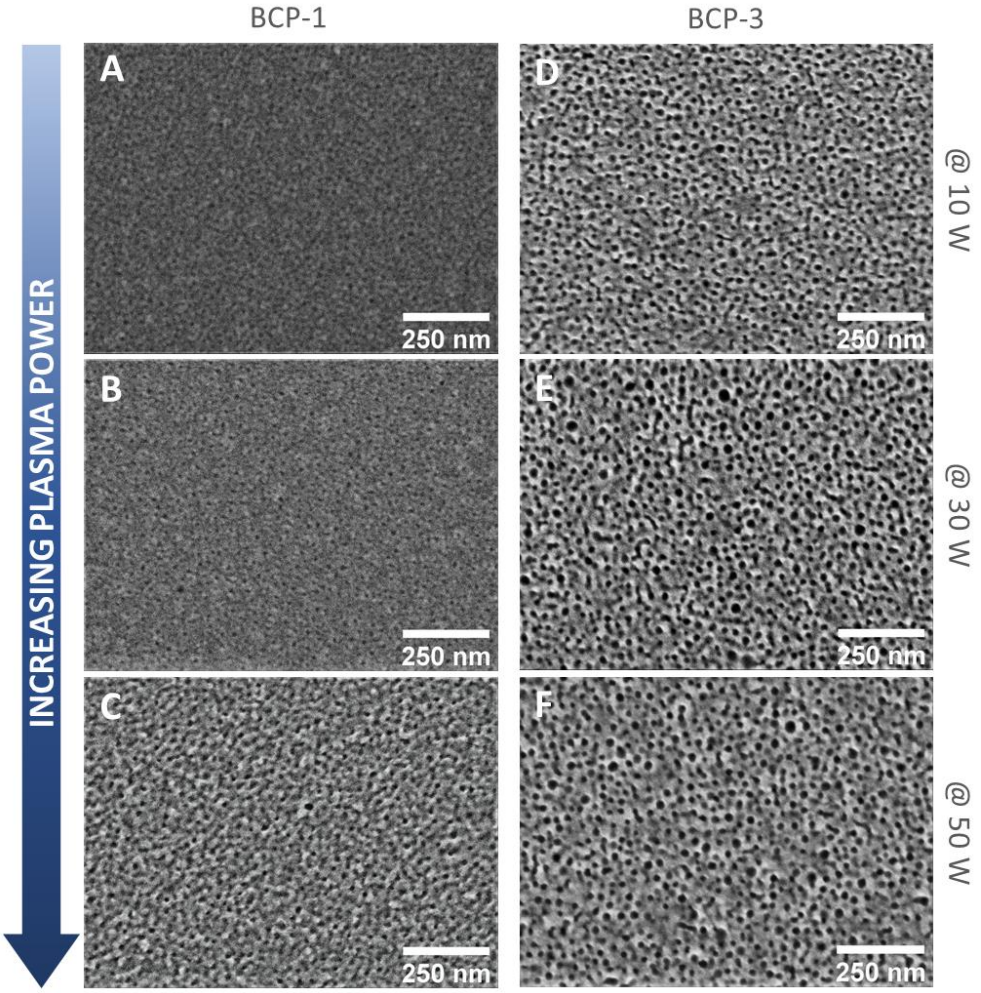

Figure S10. Effect of Ar plasma power on the structure and morphology of CuTe films. Top-view FE-SEM images of (A-C) BCP-1 film with small pores and (D-F) BCP-3 film with large pores subjected to (A, D) 10 W, (B, E) 30 W, and (C, F) 50 W Ar plasma treatment for 180 s.

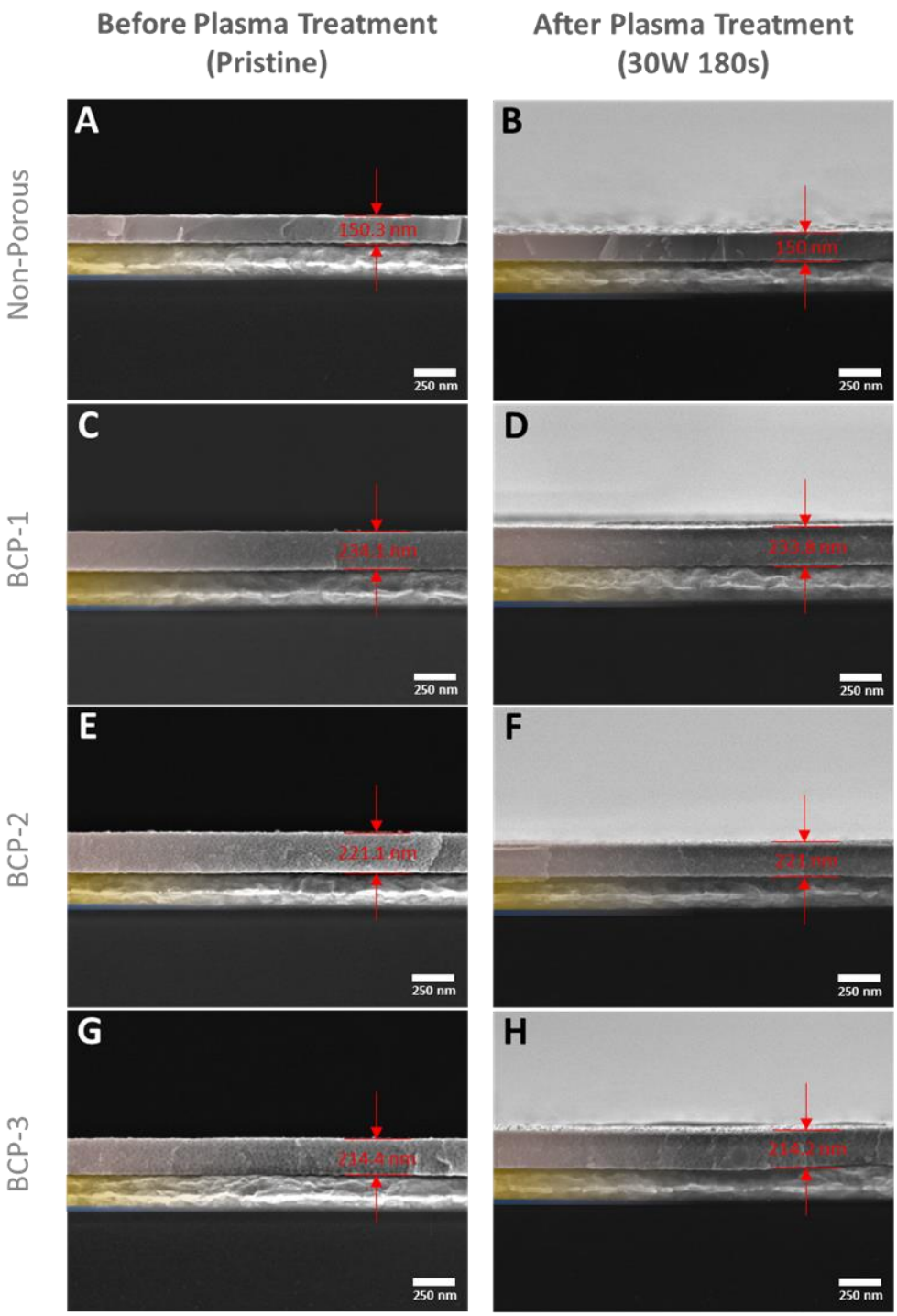

Figure S11. Cross-sectional FE-SEM images of nonporous, BCP-1, BCP-2, and BCP-3 films (A, C, E, G) before and (B, D, F, H) after 180 s of exposure to 30 W plasma power. False colors are applied: blue for Ti, yellow for Au, and brown for CuTe. Film thickness is shown on the images.

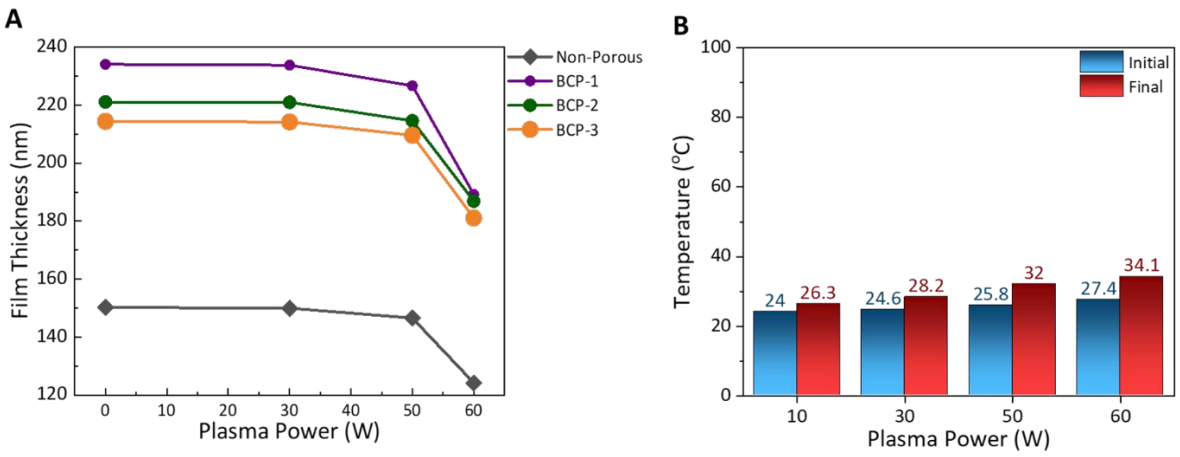

Figure S12. Effect on film thickness and process temperature due to Ar plasma treatment. (A) Film thickness of samples exposed to increasing plasma powers and (B) corresponding Ar plasma processing temperature measured at the substrate, for 180 s of plasma exposure.

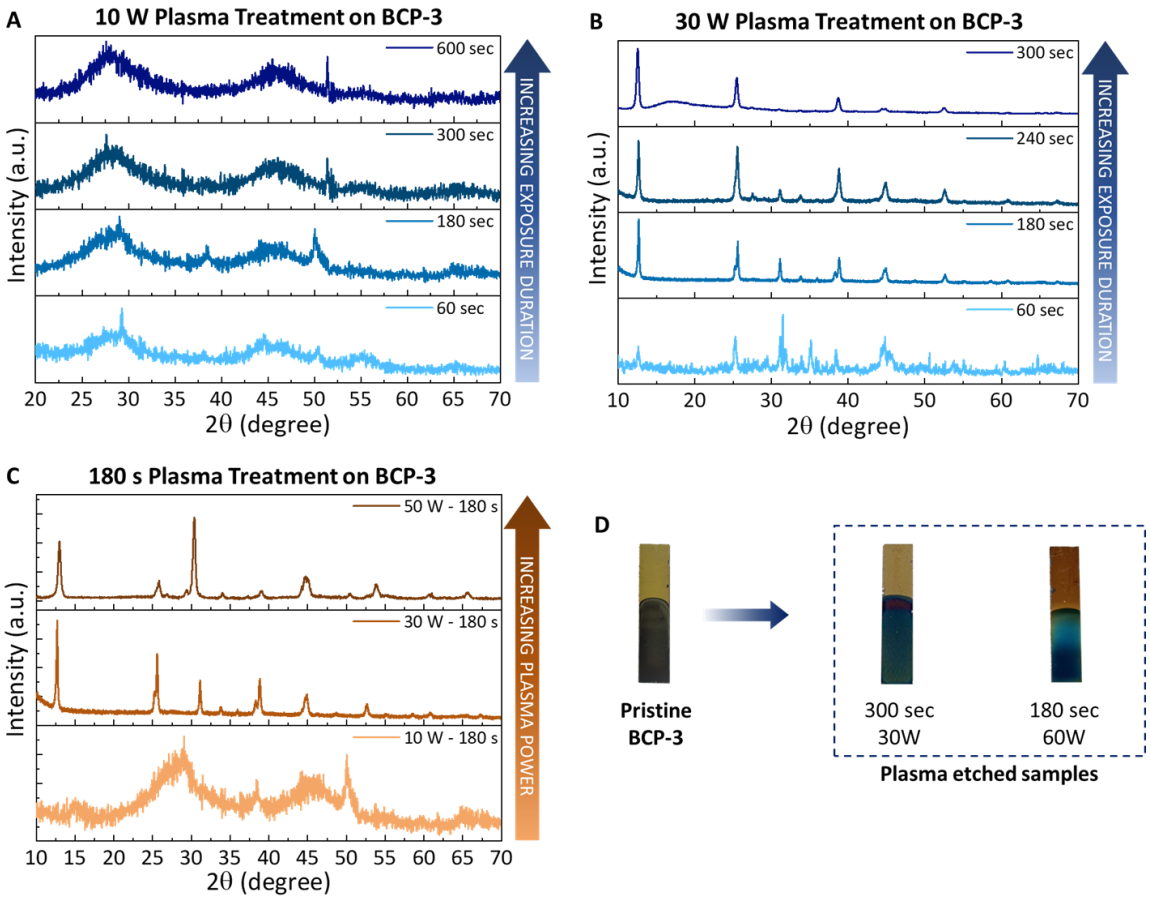

Figure S13. Effect on domain size over increasing Ar plasma exposure on BCP-3 films observed through the grazing incidence X-ray diffraction (GIXD). GIXD spectra of BCP-3 films at (A) 10 W and (B) 30 W with exposure duration increased from 60 to 300 s, and (C) at various plasma power (10, 30, and 50 W) for an exposure duration of 180 s. (D) Digital photographs of sample BCP-3 films with visible color changes after etching, either at longer exposure time or higher plasma power.

Supporting Information Note 3

Diffractogram

The out-of-plane configured GIXD on thin film samples matched well with the PDF card #01-070-8050 of vulcanite, space group *Pmmn*(59) orthorhombic crystal system for CuTe, and trace amounts of Te in the treated samples matched the PDF card #00-036-1452 of the space group *P3121*(152) hexagonal crystal system, as displayed in Figure 4B. The crystallinity (%) was calculated from the ratio of the integrated area of all crystalline peaks to the total integrated area under the XRD peaks.

Supporting Information Note 4

Optimization of plasma treatment

To determine the optimal time for the plasma treatment of mesoporous CuTe films, the compositional variation on the film surface was carefully investigated using an ion beam etching (IBE) technique with Ar gas. Based on our estimation, each etch cycle was carried out for 60 s, and the etch rate was approximately 2 nm per cycle. This slow etch rate allowed us to precisely investigate the surface oxidation and carbon contamination levels after each etch cycle. This experiment used films stored under ambient conditions for 14 d after deposition because we intentionally needed to form oxide layers on the samples. After each etch cycle, the atomic percentages of Cu 2*p*, Te 3*d*, O 1*s*, and C 1*s* were extracted and plotted from the survey scan, as shown in Figure S9. The nonporous sample in Figure S9A shows that the carbon content of the film was much higher than the oxygen content, indicating serious carbon contamination. As the films were etched gradually, carbon and oxygen contents gradually decreased, and the atomic percentages of Cu and Te increased exponentially. In the case of mesoporous CuTe films, after further IBE treatment between 120 and 240 s, the oxygen content (derived from surface oxides and hydroxides) coincided with that of Cu and Te, followed by a steep decline. From the above results, it was found that this exposure region between 120 and 240 s was an ideal operation time that could remove both carbon contamination and the oxide layer without serious etching of CuTe.

The films were then exposed to various plasma powers (10, 30, 50, 60, and 70 W) for different exposure durations. The resultant films were observed for changes in their surface states and crystalline domain sizes. From the analyzed data, the observed results exactly matched the power-law model, as shown in Figure 3B. The graph was classified into four major operational regions. Region A (green) showed that the samples exposed to these conditions had no observable improvement. In Region B, effective surface passivation and an increased domain size were observed in the mesoporous CuTe films. Beyond Region B, displacement of the surface atoms could be observed owing to the etching or sputtering process (Region D). At these levels of exposure power and duration, the collision of Ar ions is essentially inelastic, resulting in surface atom displacement. To further narrow down Region B and observe stable plasma processing conditions, Region C can be extrapolated. This region improved the crystalline domain size of the pore walls. Consequently, it was found that 30 W at 180 s of exposure was the most efficient condition.

GIXD patterns are a clear indicator of the plasma process. Figure S13 shows the GIXD patterns of the films after different plasma treatments. At 10 W exposure, the GIXD patterns showed no significant changes, even after 600 s of plasma exposure (Figure S13A). This could be due to insufficient plasma power to interact with CuTe. At 30 W of exposure, clear diffraction peaks were observed when the exposure time reached 180 s (Figure S13B). This effect is illustrated graphically in Figure 3C with changing exposure time and power. The peaks corresponded to the PDF standards of CuTe, and they were slightly altered at 300 s and above, probably owing to etching. The degree of crystallinity (%) was extracted to show that the domain sizes gradually increased with increasing exposure time. Table S3 shows an enhancement of up to 84.97% after 180 s of Ar plasma exposure (30 W), with no change in the overall film thickness when compared to the pristine samples measured by the cross-sectional FE-SEM (Figure S11 and Table S1). Any further increase in power (W) or exposure time showed no change in domain size, but a slight change in surface roughness at 50 W (Figures S10C and S10F) resulted from etching (Figures 3C and S12), accompanied by a change in the color of the film to teal blue (Figure S13D).

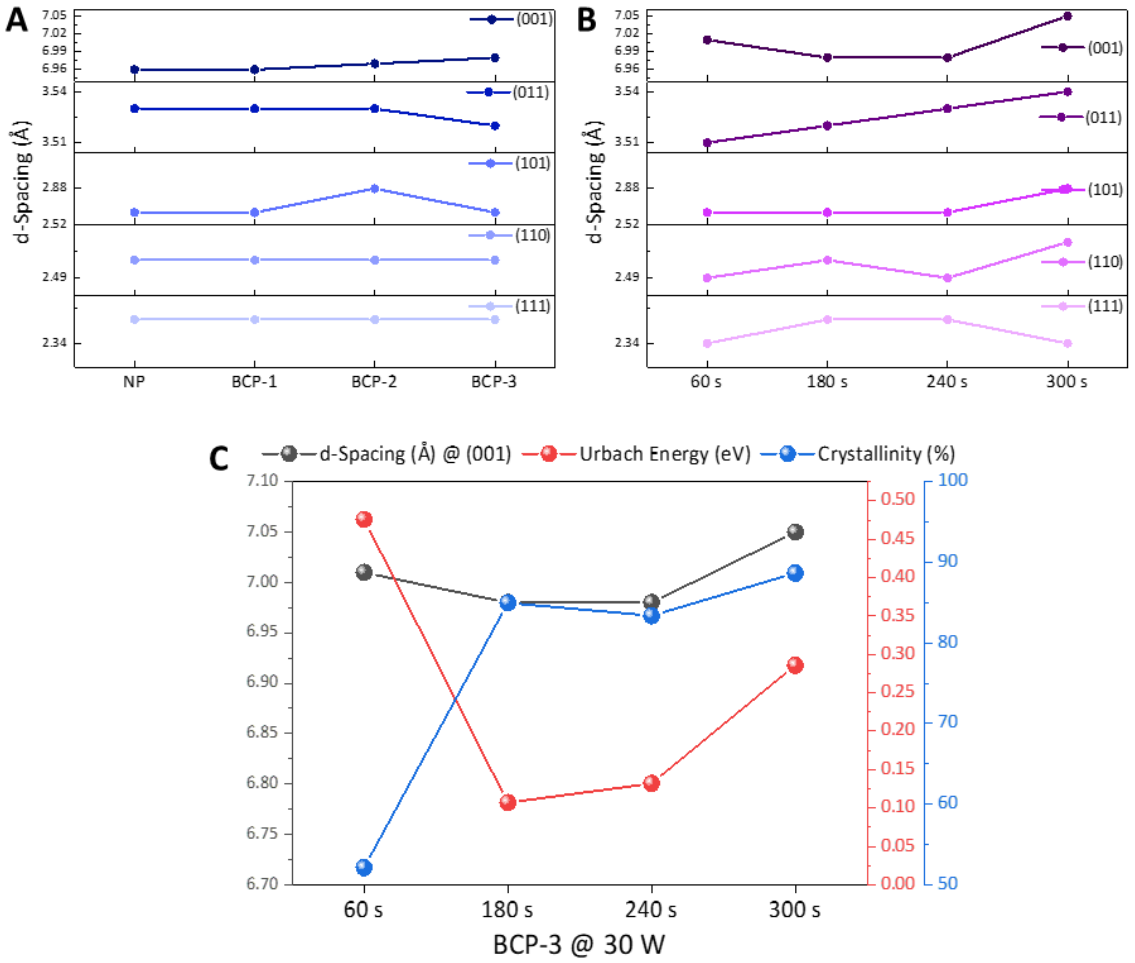

Figure S14. The *d*-spacing profiles and their correlation to E_U and Crystallinity. The *d*-spacing profiles for orientations with (A) different samples and (B) plasma treatment times (for BCP-3 film). (C) The correlation of d-spacing, E_U, and crystallinity of BCP-3 film with different plasma treatment times (plasma power = 30 W).

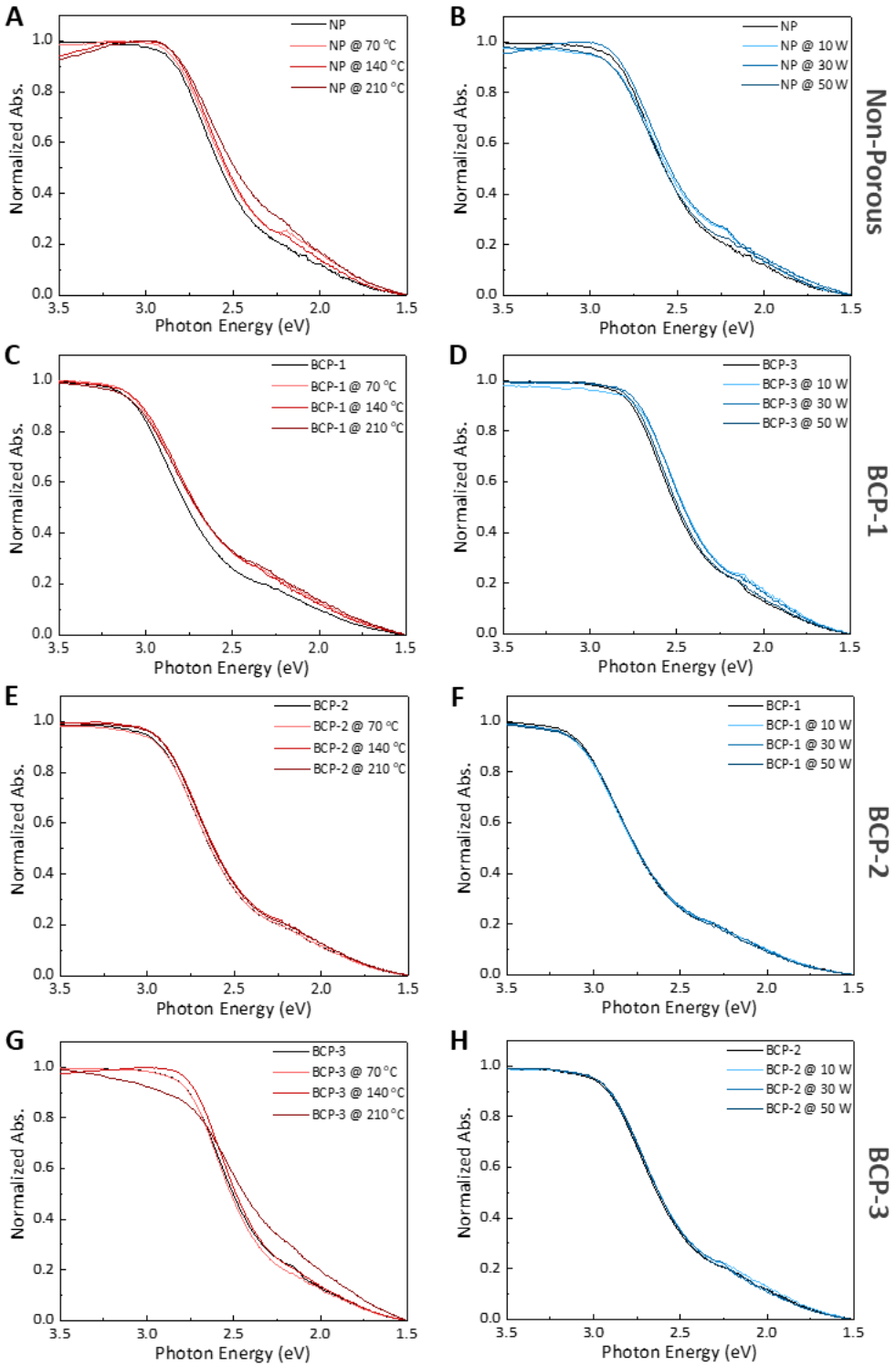

Figure S15. Normalized absorbance *vs*. photon energy of CuTe films. Absorbance of (A, B) NP, (C, D) BCP-1, (E, F) BCP-2, and (G, H) BCP-3 films after (A, C, E, G) thermal and (B, D, F, H) plasma treatment.

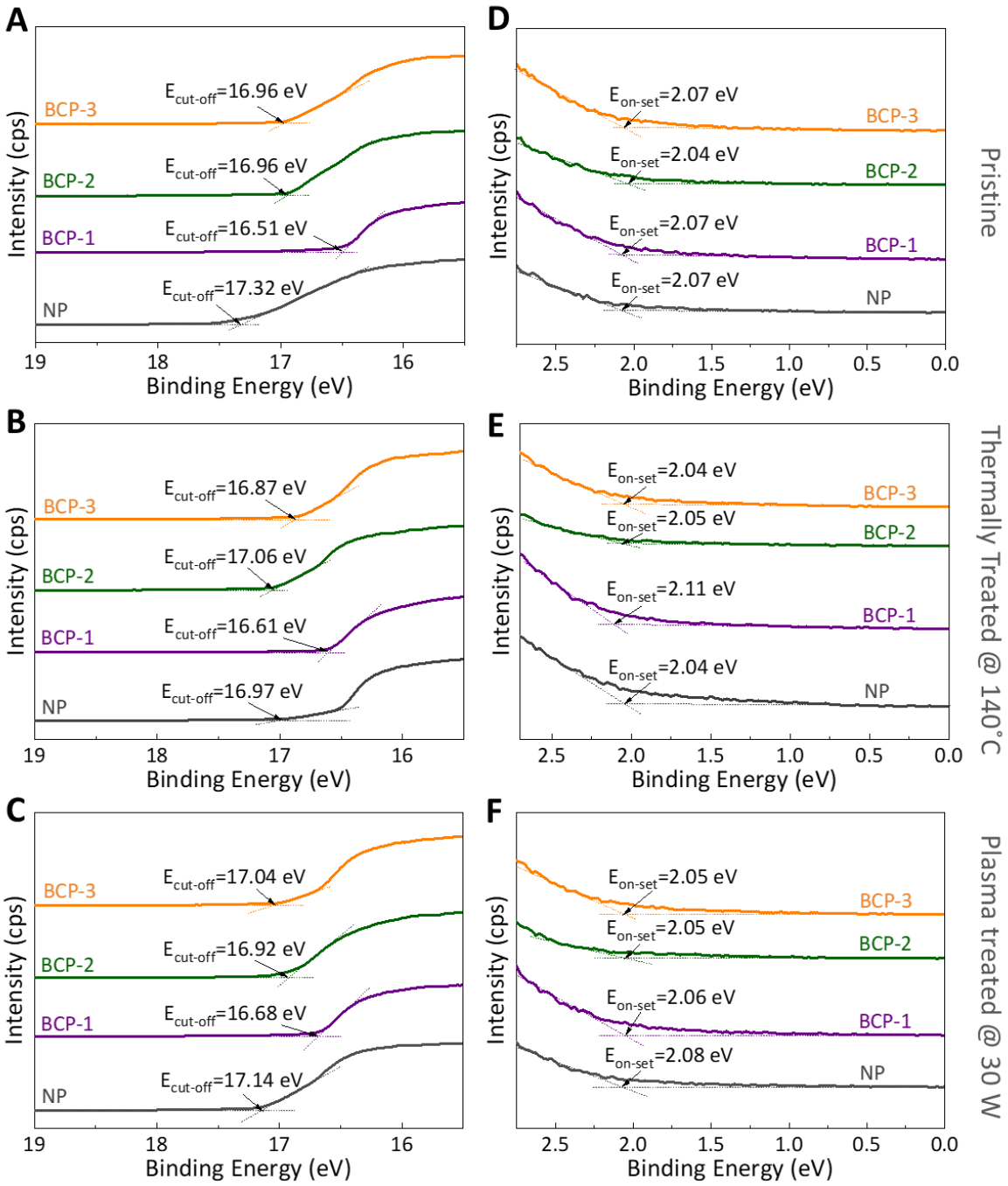

Figure S16. UPS analysis to understand work-function and HOMO of NP and mesoporous films exposed to thermal and plasma treatment. Cut-off and on-set energies of (A, D) pristine, (B, E) 140 °C thermally treated, and (C, F) 30 W plasma treated films, respectively.

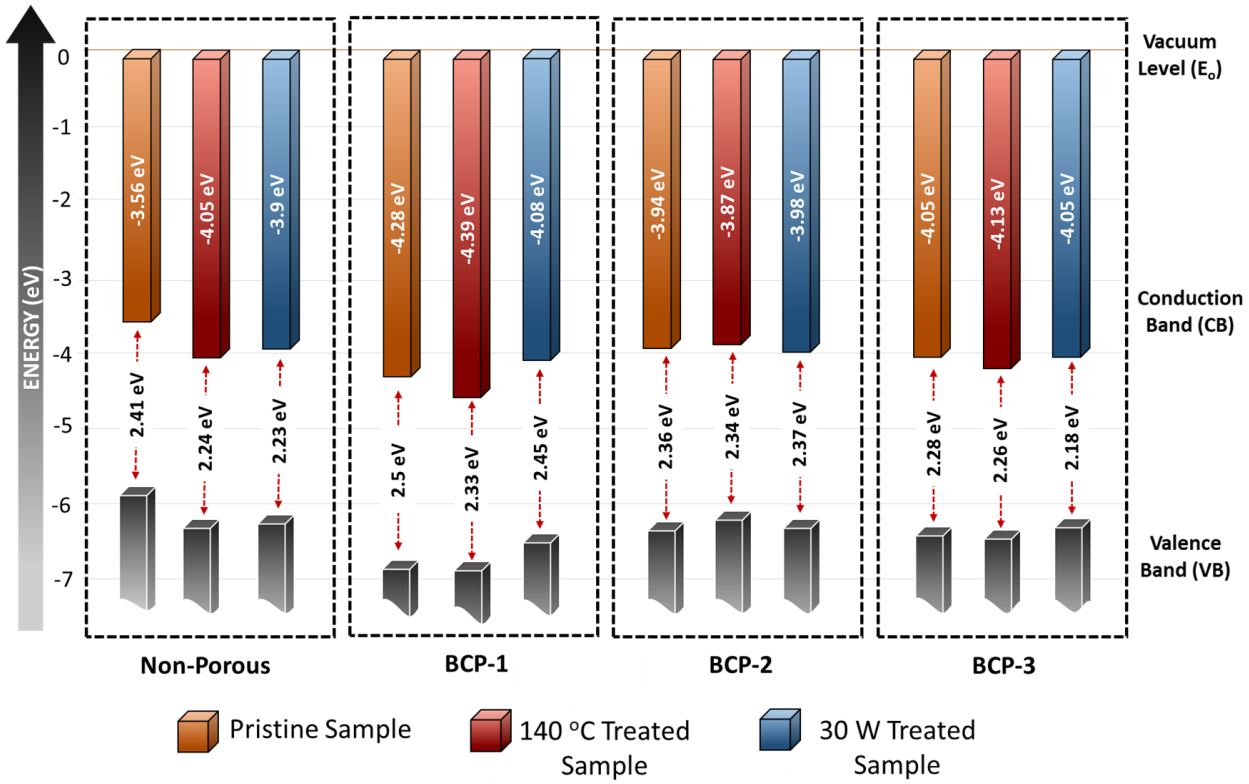

Figure S17. Illustration of changes in the bandgap of NP, BCP-1, BCP-2, and BCP-3 films, before treatment (pristine), and after 140 °C thermal or 30 W plasma treatment, respectively.

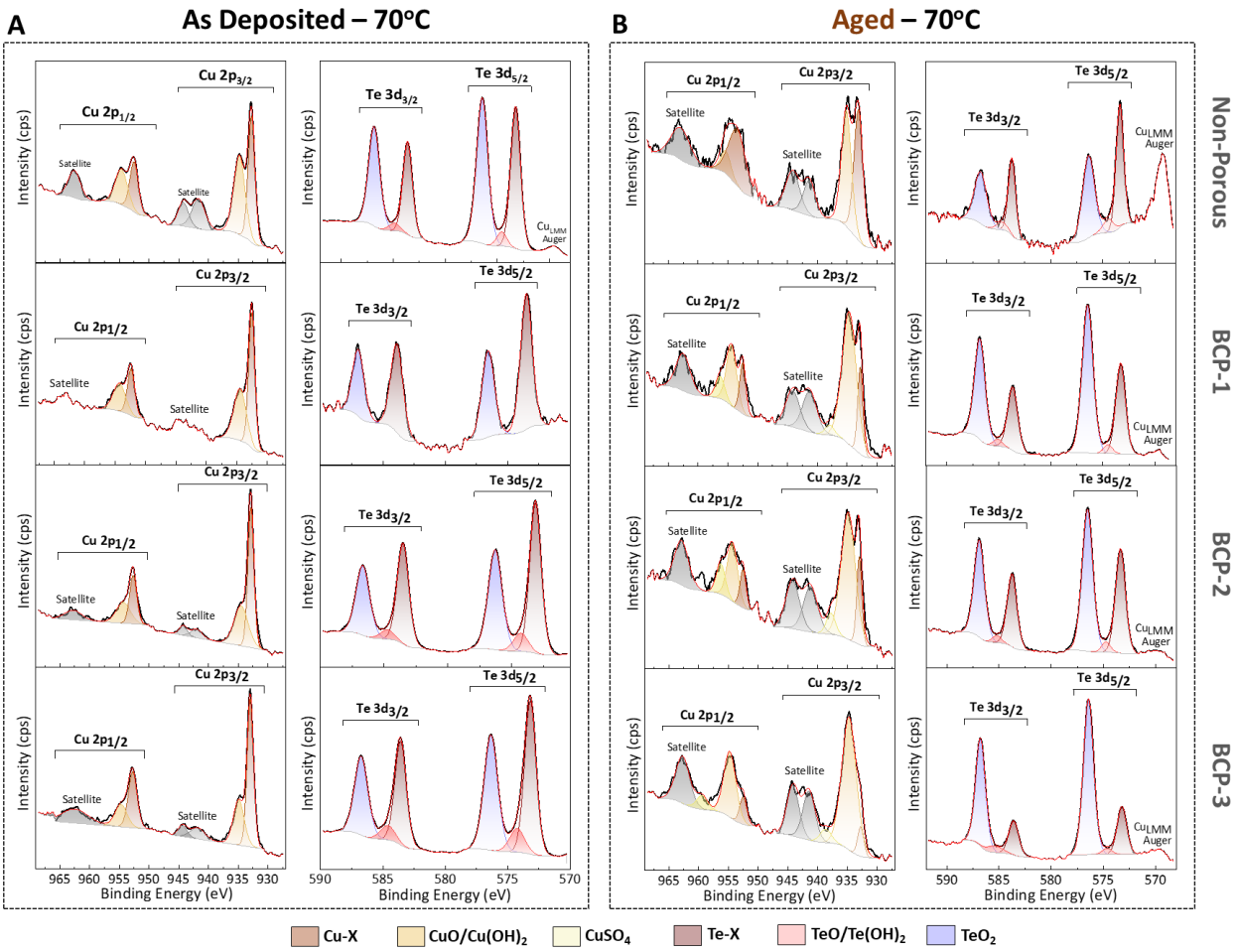

Figure S18. Core-level XPS spectra of Cu 2*p* and Te 3*d* peaks to demonstrate the effective changes in surface oxidation after post-annealing. CuTe films measured immediately (A) after 70 °C post-annealing and (B) the same samples after aging for 200 days.

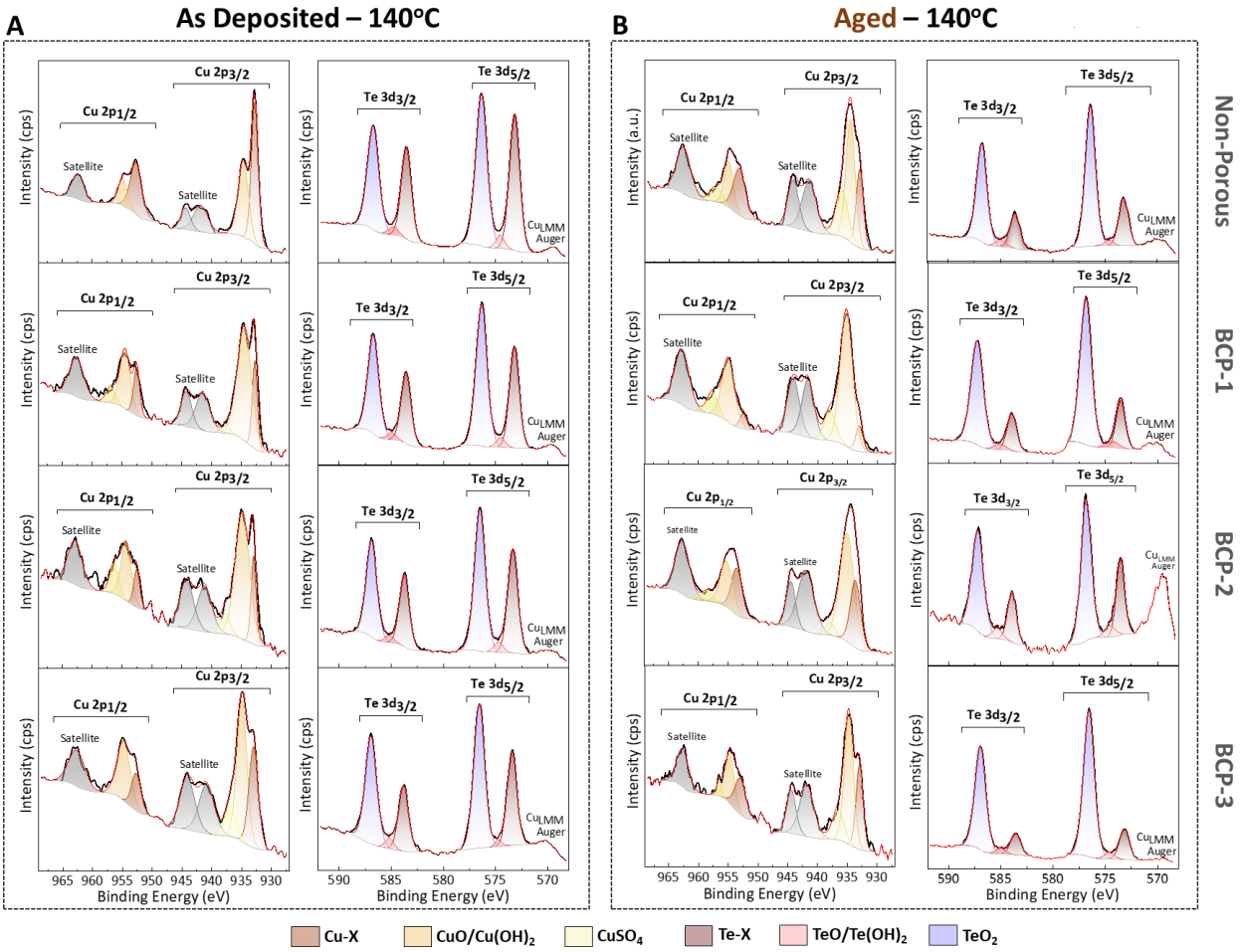

Figure S19. Core-level XPS spectra of Cu 2*p* and Te 3*d* peaks to demonstrate the effective changes in surface oxidation after post-annealing. CuTe films measured immediately (A) after 140 °C post-annealing and (B) the same samples after aging for 200 days.

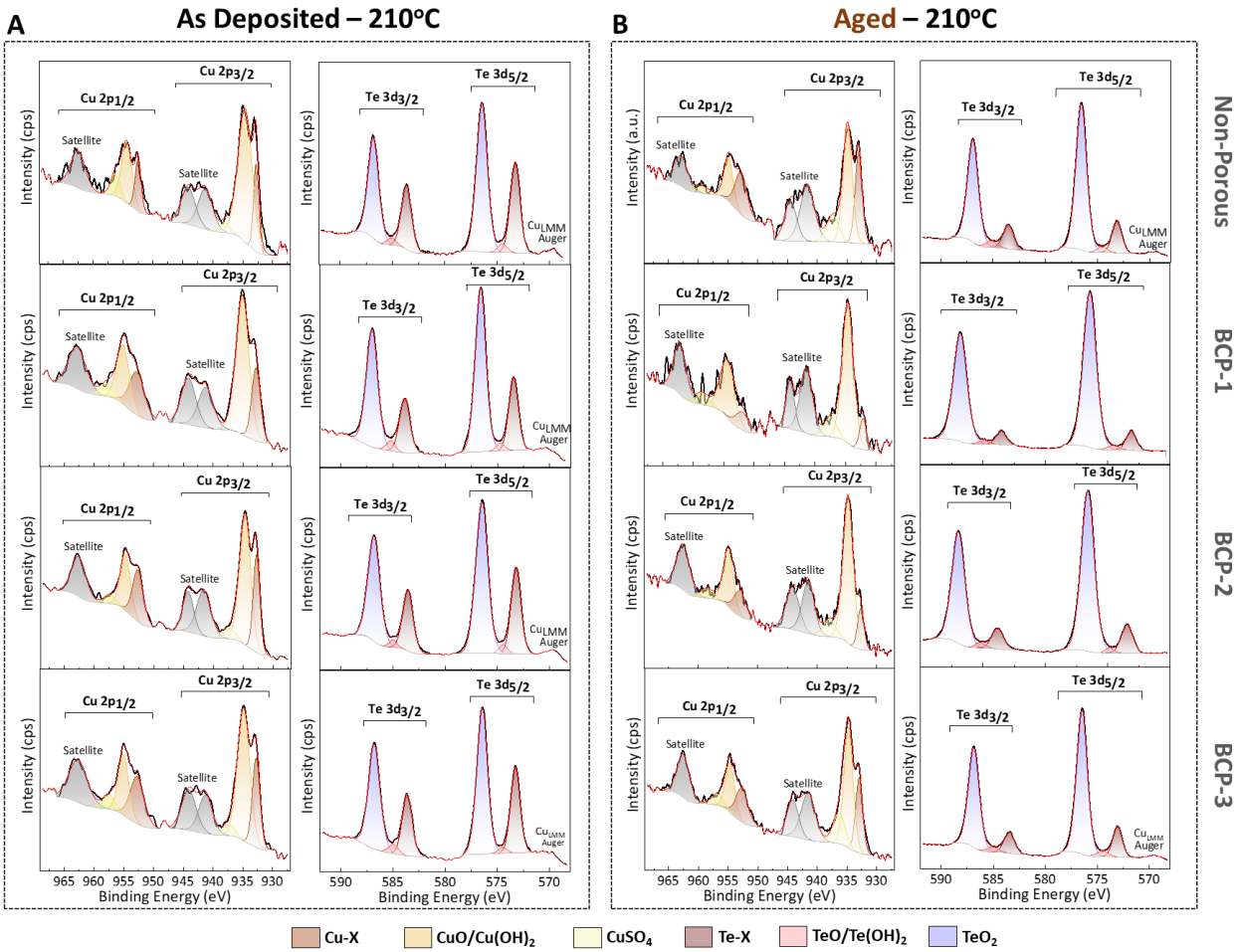

Figure S20. Core-level XPS spectra of Cu 2*p* and Te 3*d* peaks to demonstrate the effective changes in surface oxidation after post-annealing. CuTe films measured immediately (A) after 210 °C post-annealing and (B) the same samples after aging for 200 days.

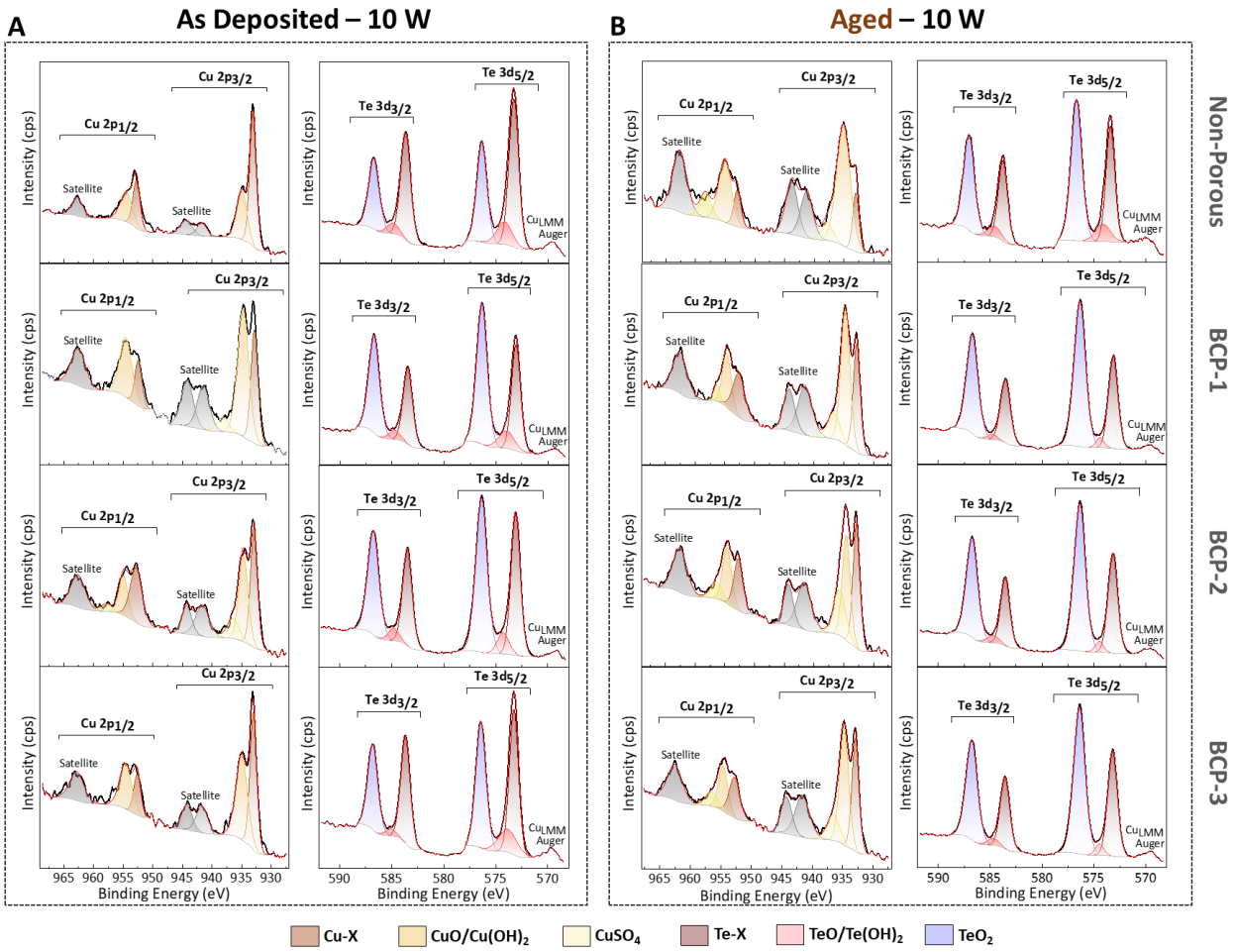

Figure S21. Core-level XPS spectra of Cu 2*p* and Te 3*d* peaks to demonstrate the effective changes in surface oxidation after plasma treatment. CuTe films measured immediately (A) after 10 W plasma treatment and (B) the same samples after aging for 200 days.

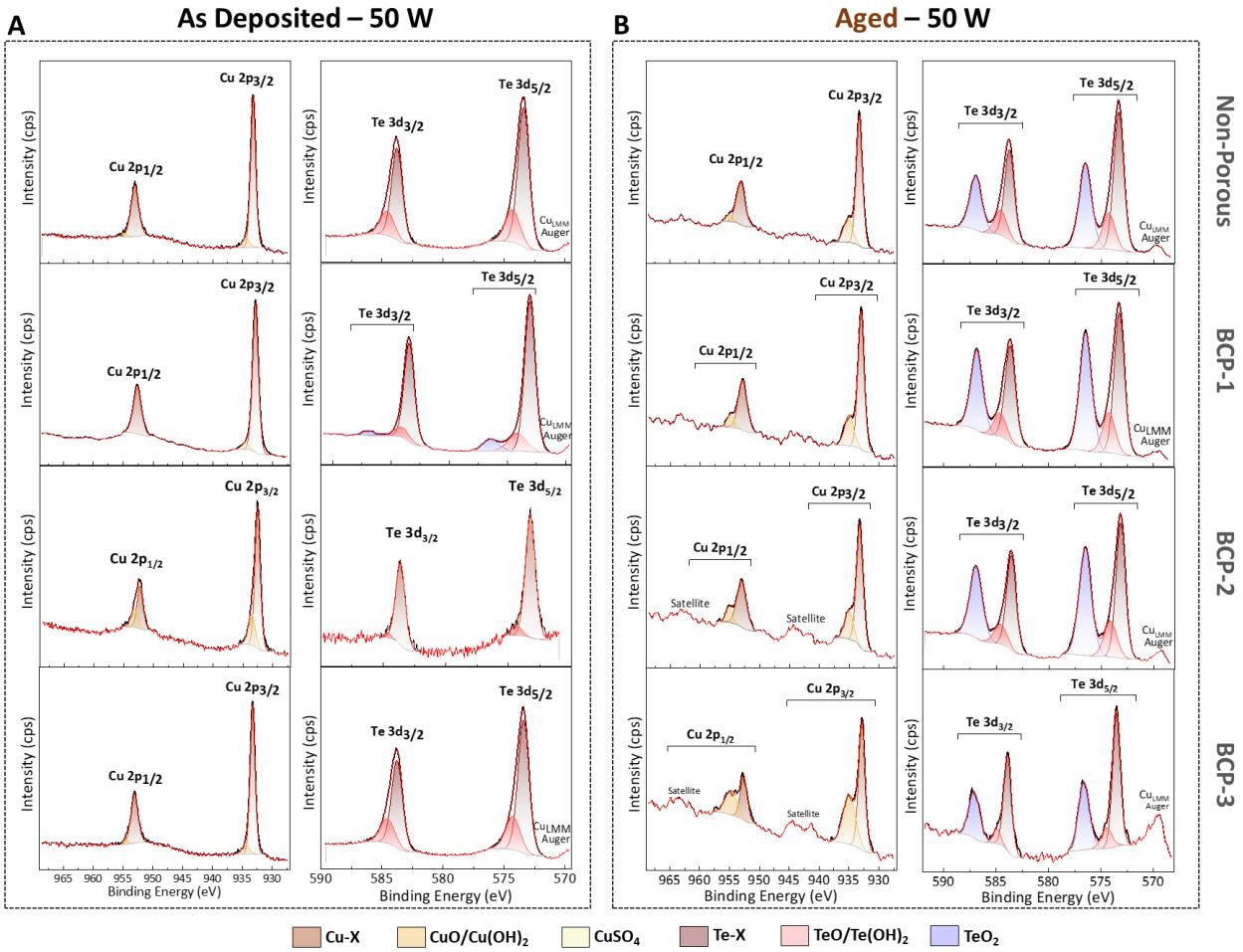

Figure S22. Core-level XPS spectra of Cu 2*p* and Te 3*d* peaks to demonstrate the effective changes in surface oxidation after plasma treatment. CuTe films measured immediately (A) after 50 W plasma treatment and (B) the same samples after aging for 200 days.

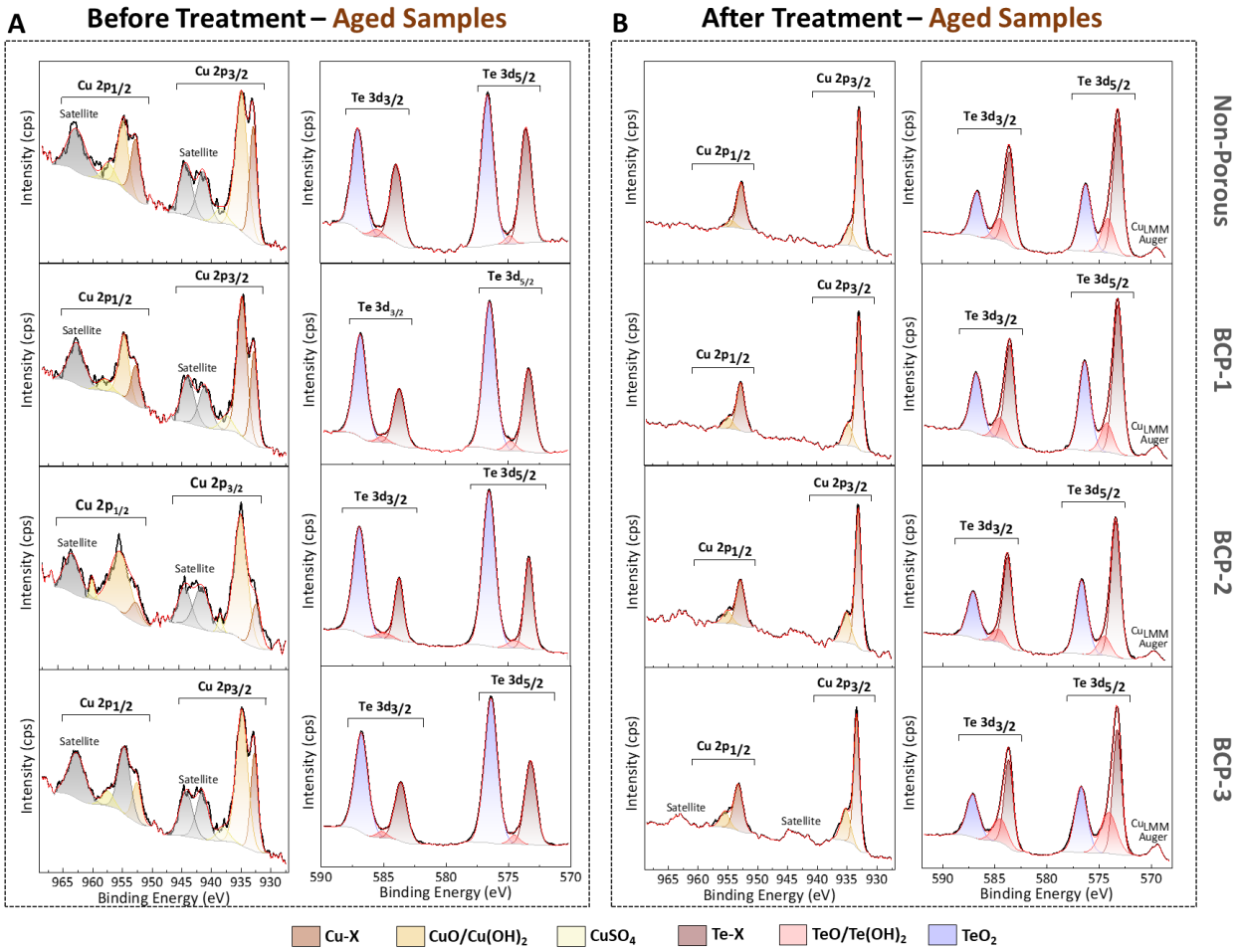

Figure S23. Core-level XPS spectra of Cu 2*p* and Te 3*d* peaks for aged samples demonstrating surface oxidation after plasma treatment. (A) Pristine CuTe films (before treatment) and (B) after 30 W plasma treatment.

Supporting Information Note 5

X-ray photoelectron spectroscopy

XPS analysis was performed using the high-resolution spectra of the Cu 2*p* and Te 3*d* peaks to analyze the surface oxidation of CuTe. All the peaks were calibrated for C 1*s* (285 eV). The core-level spectra of the exposed and aged samples with different thermal treatments (70, 140, and 210 °C in a vacuum oven) and plasma power treatments (10, 30, and 50 W in an Ar environment) were deconvoluted with uniform color codes to distinguish the peaks, as indicated below each graph (Figures S18–S23).

The $2p_{3/2}$ and $2p_{1/2}$ splitting of Cu 2*p* were deconvoluted at binding energies for Cu-X (derived from CuTe) positioned at 932.9 and 952.7 eV with 19.8 eV difference in binding energy. Cu(II)O/Cu(II)$(OH)_2$ peaks were located at 934.6 and 954.65 eV, indicating the formation of oxide layer. Cu(II)SO_4 peaks (from unreacted precursor solution) were also observed at 937.26 and 957.76 eV.[2] In contrast, the $3d_{5/3}$ and $3d_{3/2}$ splitting of Te 3*d* were deconvoluted to Te-X (derived from CuTe) positioned at 572.91 and 583.3 eV with 10.39 eV difference in binding energy. Te(IV)O_2 peaks were found at 576.07 and 586.44 eV, with trace amounts of other Te oxide layers such as Te(II)O/Te(II)$(OH)_2$ at 573.78 and 584.25 eV.

The core-level spectra of the Cu 2*p* and Te 3*d* peaks of the pristine and aged films are shown in Figures S18–S23. For accurate spectral measurements, the as-prepared pristine films were analyzed immediately after washing. The aged films were prepared by storing the pristine films under ambient conditions for 200 d. This aging process allowed the sample surface to react with ambient gases and to demonstrate the stability of the films. The atomic percentages of Cu(II)O/Cu(II)$(OH)_2$ in Cu 2*p* and TeO_2 in Te 3*d* indicate the intensity of the surface oxidation. These values were precisely extracted by deconvoluting the core spectra. In the case of the pristine films, the intensity of oxidation in the NP film explained the inherent nature of the material. The material reacted easily to ambient conditions because of the termination of atoms at the surface of the films. A spike in the oxidation level was observed because of the increase in the exposed surface area by mesopores. The smaller the pore size, the larger was the surface area with unsaturated surface states. After thermal treatment at 70 °C, the surface oxidization intensity of the film was reduced without any change in morphology (Figures S7 and S18A); however, this temperature was sufficient to initiate the diffusion of surface-adsorbed atoms during aging (Figure S18B). In contrast, when the temperature was increased to 140 and 210 °C, the original mesoporous structure started to collapse (Figure S7). As the temperature increased, the diffusion rate of surface-adsorbed atoms accelerated into the pore walls because of the higher surface energy than that of the NP films. After being brought back to room temperature, the surface energy of the films remained slightly higher, making them readily react with ambient gases, as observed in the corresponding XPS spectra (Figures S19 and S20). Upon aging, these films remained reactive to ambient gases, increasing the oxide layer thickness along the surface, which was indicated by the presence of intense Cu(II)O/Cu(II)$(OH)_2$ and TeO_2 peaks. After high-temperature treatments, the films with smaller pore sizes showed significantly higher oxidization rates than those with larger pore sizes because of their thinner walls with higher reactive sites (Table S5). These results

indicated that the thermally treated films formed an oxide layer of 5–10 nm thickness along the surface during aging; therefore, it was difficult to probe the presence of CuTe within the pore walls.

In the case of the plasma treatment, the chemically inert Ar gas remained unreactive and pacified the surface of the films at sufficient plasma power, as discussed in Supporting Information Note 4. At 10 W plasma treatment, the energy was insufficient to completely pacify the surface, which was evident from the spectra observed after 10 W of exposure, showing no significant change in the oxide level (Figure S21). In contrast, by increasing the power to 50 W, the Ar ions gained sufficient energy to gently displace the surface atoms. However, owing to the intense exposure energy at 50 W, rapid etching occurred simultaneously with domain size improvement, making it difficult to optimize suitable plasma treatment conditions by controlling the exposure duration before the appearance of etching (Figure S22A). Furthermore, after aging, they were oxidized gradually in the 50 W plasma treated samples, as the Ar ions collided inelastically, causing etching upon each successive collision on the surface (Figure S22B). Similarly, the pristine films after aging showed a relative increase in the surface oxide levels compared to those before aging (Figure S23A and Table S5). While exposing the films to an optimal plasma power (30 W), the pre-existing oxide layer formed during transportation and handling was eliminated by elastic collisions caused by the Ar ions under controlled exposure conditions. Therefore, the oxidation rate of the films exposed to 30 W was relatively lower than that of the films exposed to other plasma powers (Figure S23B and Table S5).

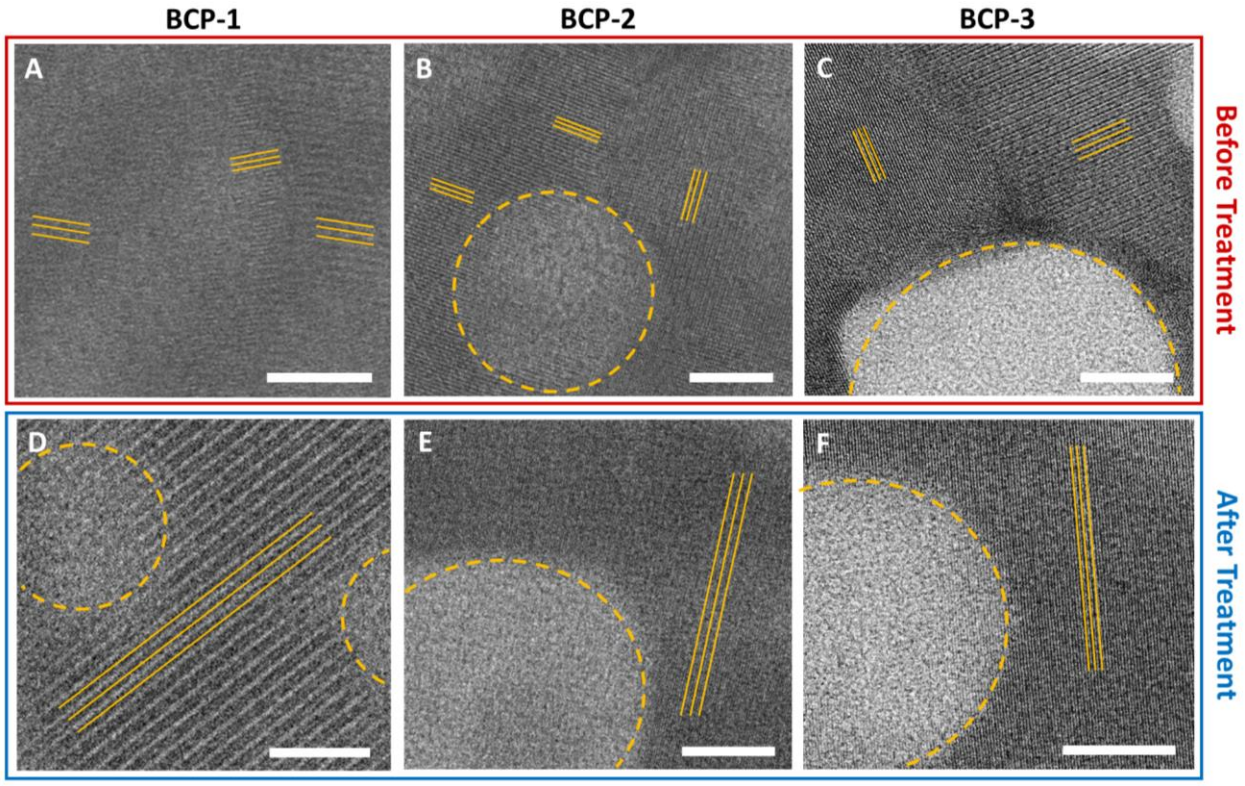

Figure S24. Cross-sectional STEM images at lattice level. Cross-sectional STEM-BF images at higher magnification on (A, D) BCP-1, (B, E) BCP-2, and (C, F) BCP-3 films before (within red outline) and after 30 W plasma treatment (within blue outline). Plasma treatment resulted in crystallinity enhancement, indicated by yellow lines along the lattice. Samples before treatment show lattice orientation at different angles, which were rearranged after optimal plasma treatment (scale bar: 5 nm).

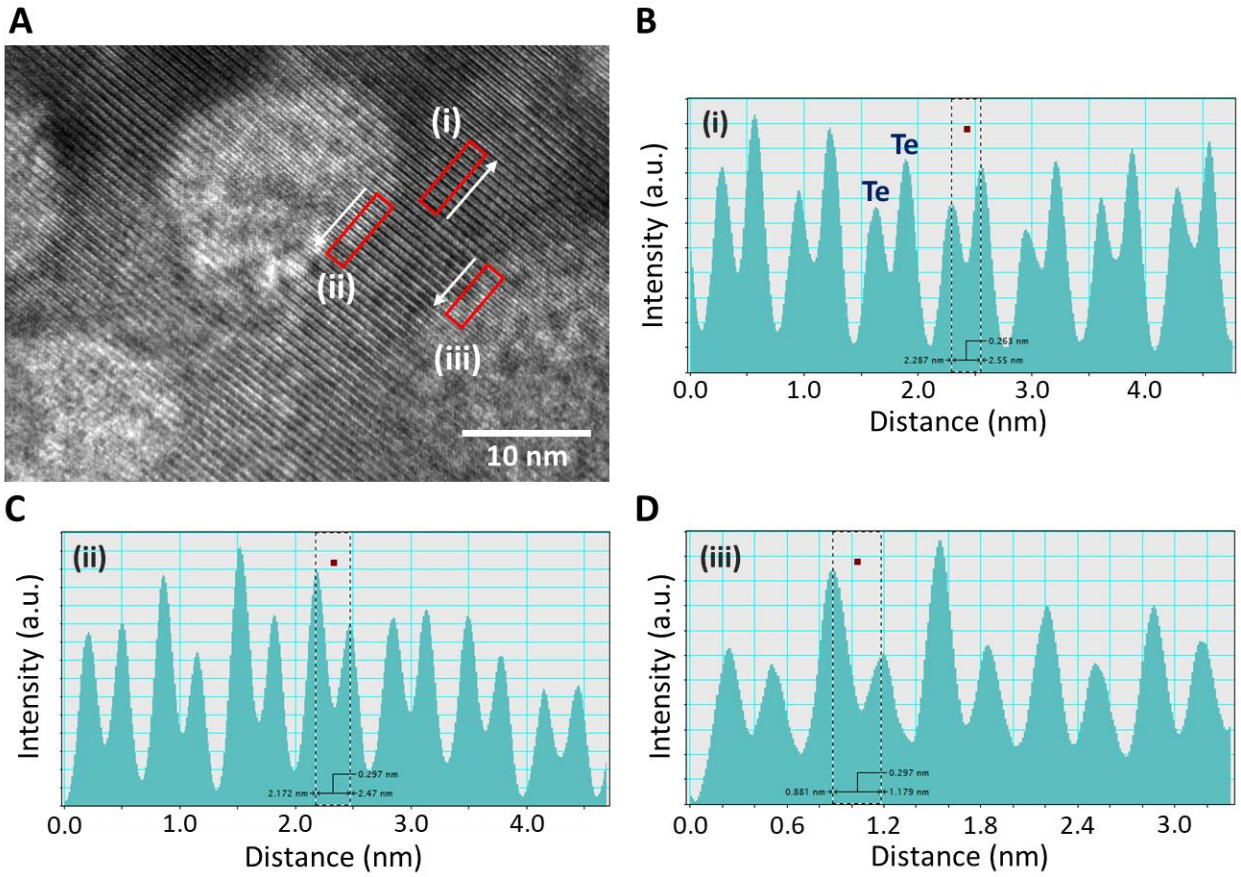

Figure S25. High resolution **(**HR**)**-TEM and *d*-spacing analysis on BCP-3 film. (A) HR micrograph of BCP-3 with three positions indicated for extracting changes in *d*-spacing of the indicated integral areas (B) i, (C) ii, and (D) iii.

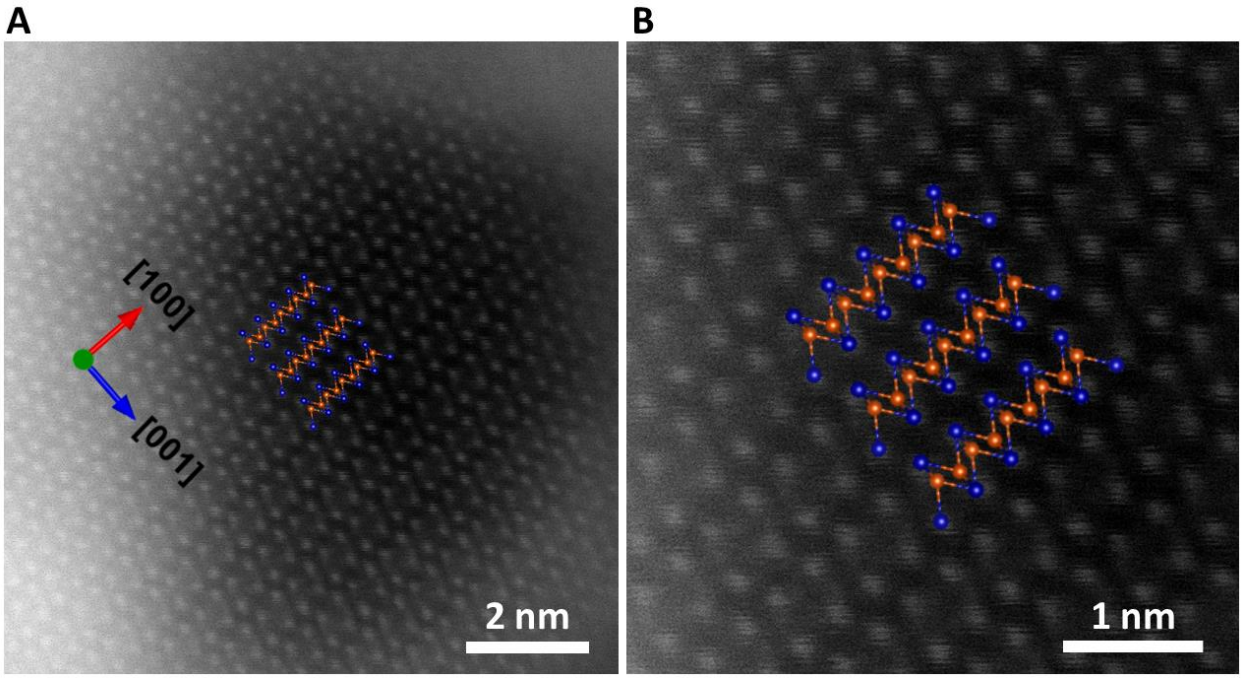

Figure S26. HR-STEM and orthorhombic crystal along zone axis [010]. HR-HAADF image of (A) BCP-1 film oriented along zone axis [010] as indicated with (B) high magnified image.

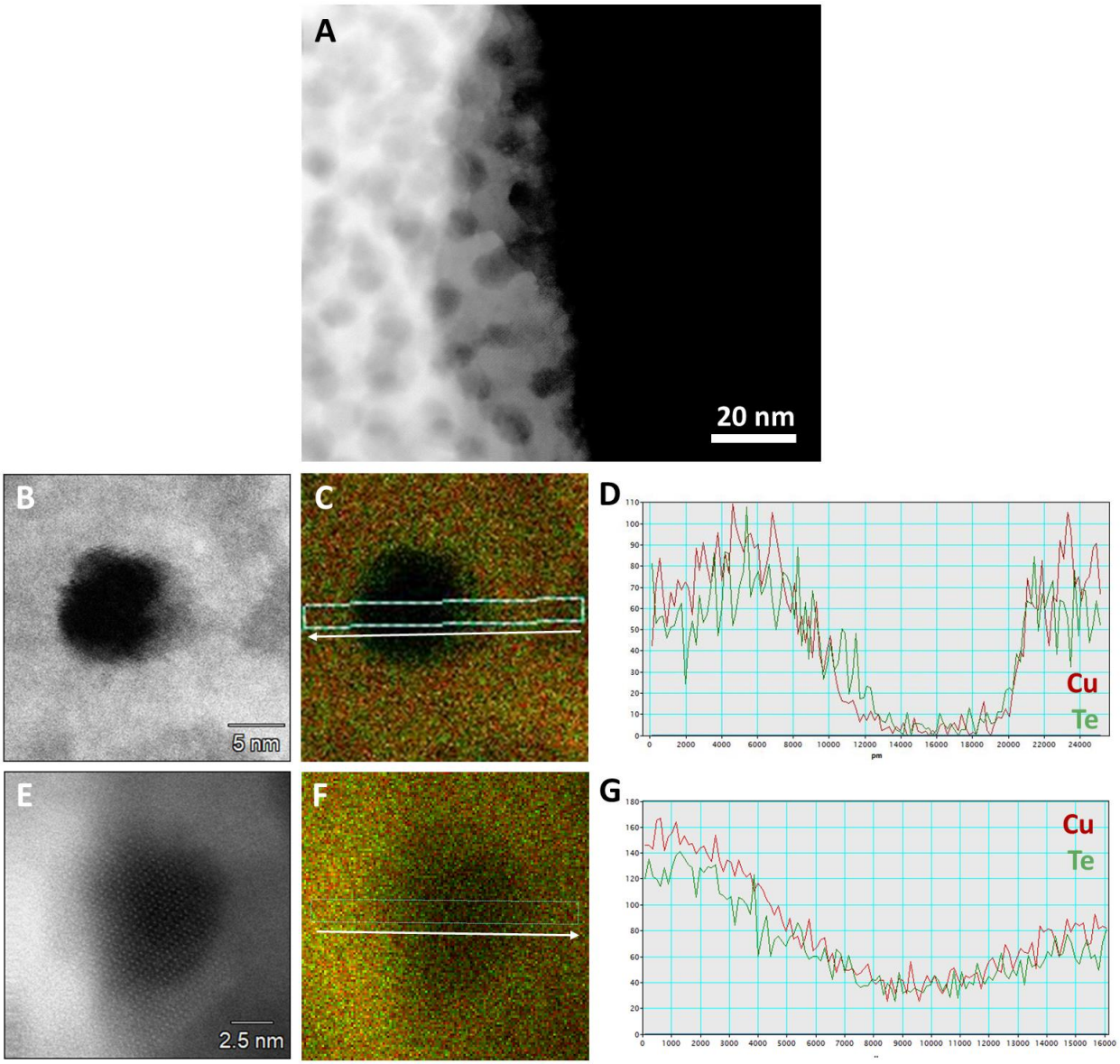

Figure S27. HAADF-STEM images, EDX mapping images, and EDX line scanning profiles of plasma treated BCP-1 film. (A) HAADF-STEM images and (B, E) high-resolution images along a pore. (C, F) EDX mapping images and (D, G) EDX line profile images across a pore directed along the white arrow. Cu and Te indicate in red and green, respectively.

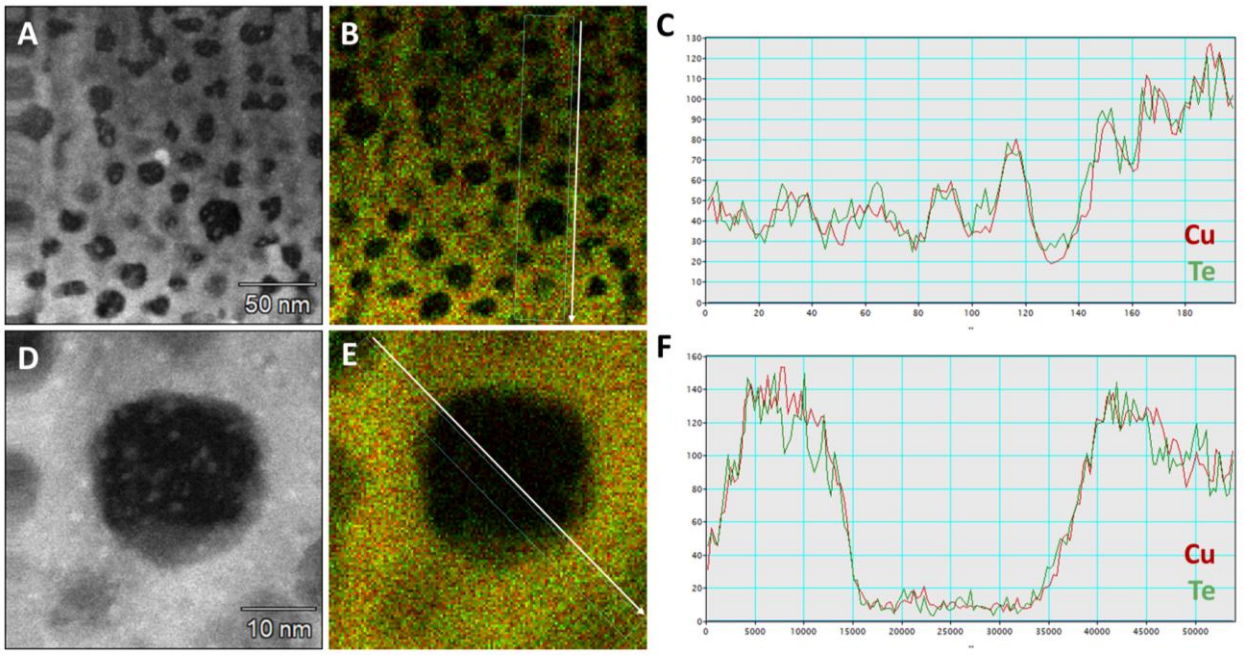

Figure S28. HAADF-STEM images, EDX mapping images, and EDX line scanning profiles of plasma treated BCP-2 film. (A, D) HAADF-STEM images, (B, E) EDX mapping images and (C, F) EDX line profile images across pores directed along the white arrow. Cu and Te indicate in red and green, respectively.

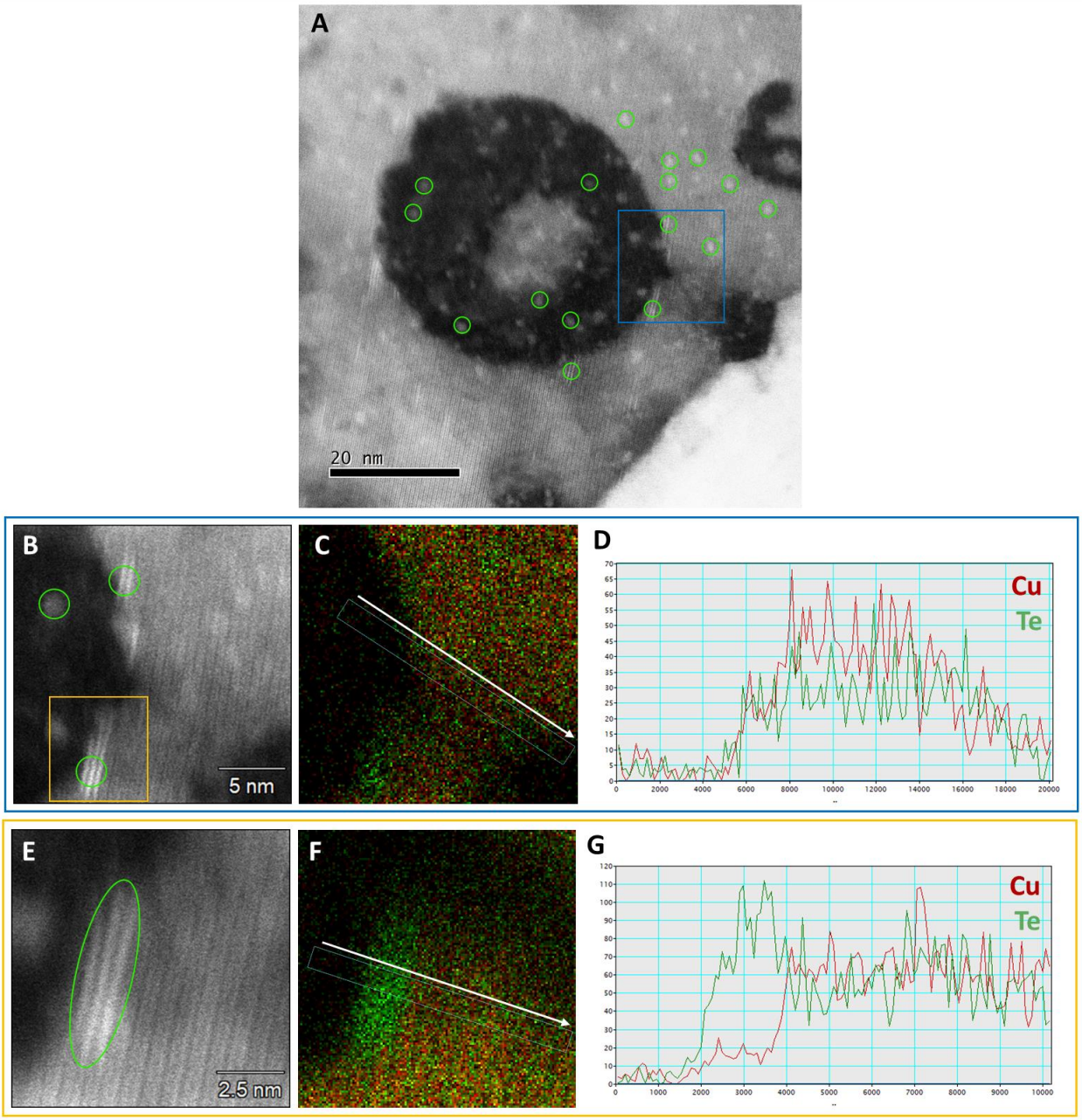

Figure S29. HAADF-STEM images, EDX mapping images, and EDX line scanning profiles of plasma treated BCP-3 film. (A, B, E) HAADF-STEM images, (C, F) EDX mapping images, and (D, G) EDX line profile images across pores directed along the white arrow. Cu and Te indicate in red and green, respectively.

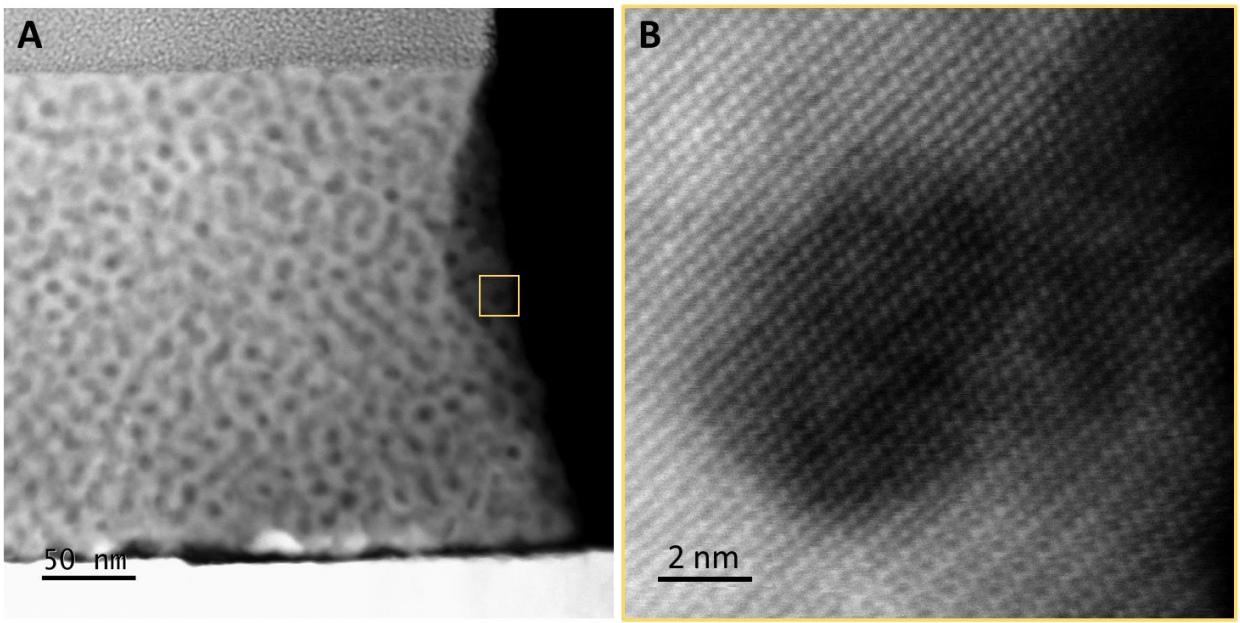

Figure S30. HAADF-STEM images on plasma treated BCP-1 film. (A) HAADF-STEM image and (B) high-resolution image showing no localized Te nanoclusters.

Supporting Information Note 6

TEM study

When the CuTe films were treated thermally, the original pore structures were distorted, and a further increase in the temperature caused the structures collapsed completely (Figures S7 and S8). Through a careful HAADF-STEM study, the cross-sectional sample observed at elevated temperatures revealed the migration of Cu atoms towards the Au substrate, leaving excess Te observed by the EDX compositional map (Figure S8). These analyses indicated that, at elevated temperatures (140 °C and above), the diffusion rate of Cu or its solubility in Au increased.

Post-processing in the presence of a sufficiently strong electric field between two parallel plates generates plasma, which is a column of ionized gases. The plasma sheath interacted perpendicularly with the sample surface and was maintained at the opposite potential. For a better electrical pathway, the non-sampling regions of the electrode were masked. This directed the lattice arrangement in the walls to be oriented vertically from the substrate. These orientations formed the shortest charge transport pathway for plasma ions to interact with the electrode maintained at the opposite potential.

A previous report demonstrated that highly crystalline 2D materials were synthesized under such plasma conditions and oriented vertically to the substrates.[3,4] Figure S24 shows STEM images of BCP-1, BCP-2, and BCP-3 films at higher magnifications, indicating a change in the lattice orientation before and after plasma treatment. The sample exposed to optimal Ar plasma showed very small widening (2.97 Å) in *d*-spacing between Cu and Te atoms along the pore, whereas the *d*-spacing value inside the wall was measured to be 2.63 Å (Figure S25), as a result of mesoporous architecture (with a small difference of 0.34 Å). Figure S26 shows the atomic resolution of CuTe along the [010] zone axis for BCP-1 film, with an overlaid orthorhombic crystal structure. Overall, from GIXD, the average *d*-spacing values matched the values observed in the TEM images. The plasma treated films showed an enhancement in domain size oriented along the [100] zone axis perpendicular to the substrate, as discussed in the main section. HAADF-STEM images of the Ar plasma treated mesoporous films with different pore sizes are shown in Figures S27–S30. Elemental mapping and line-scanning analysis revealed that each element (Cu and Te) was uniformly distributed in the pore walls. In particular, for BCP-3 film with a large pore size, several bright spots were observed on the pore surface and in the bulk, indicating the formation of Te aggregates (Figure S29). The presence of Te aggregates was confirmed by XPS analysis and GIXD (Figures 4B and D). However, these sites were not widely distributed in BCP-1 film with a small pore size (Figure S30).

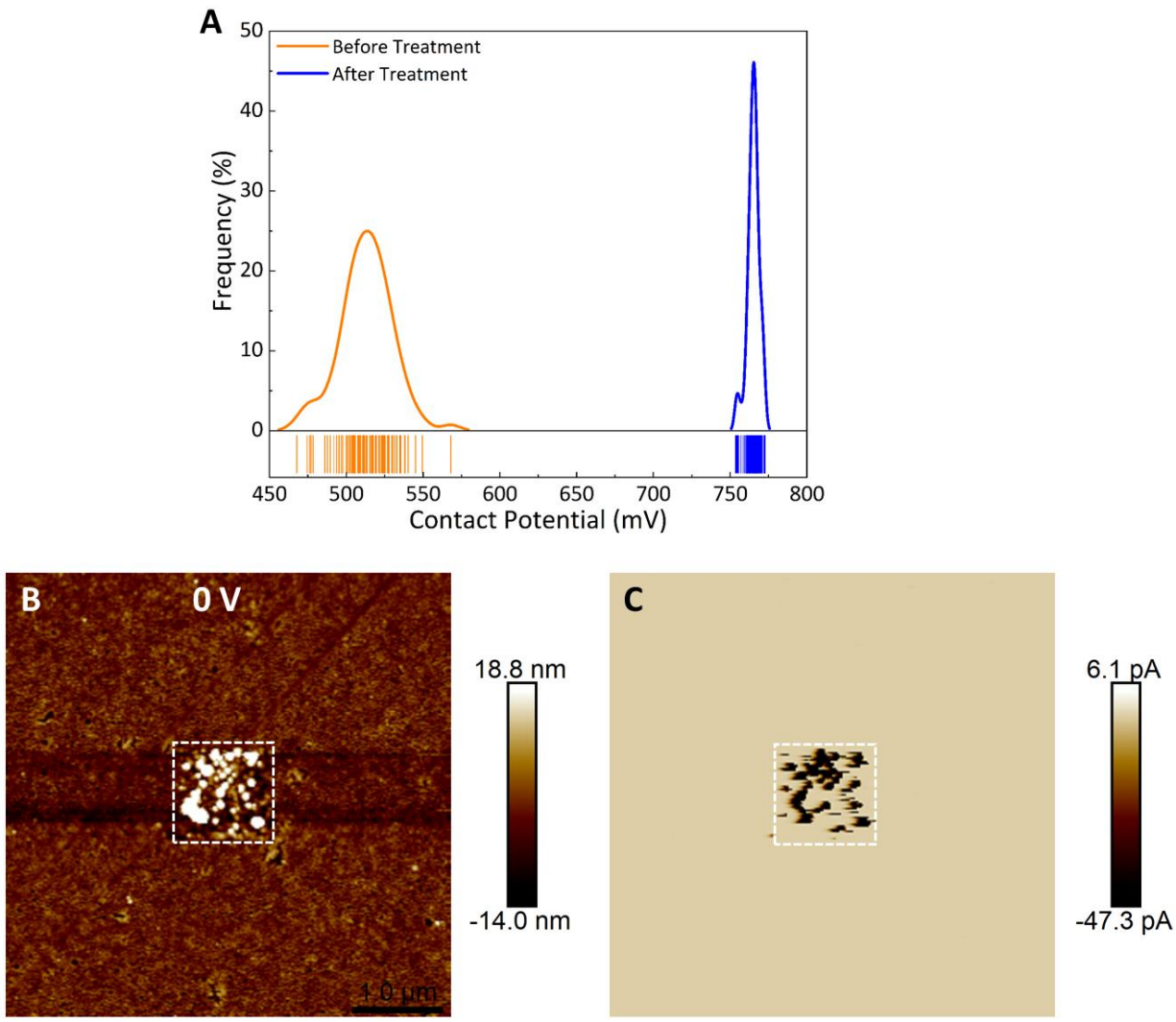

Figure S31. PF-TUNA on the BCP-3 film. (A) Contact potential distribution on a 1 µm × 1 µm area before and after treatment. The effect of applied potential mapped across the indicated 5 µm × 5 µm area causing retention of charges over other areas observed by (B) topography and (C) TUNA current profile.

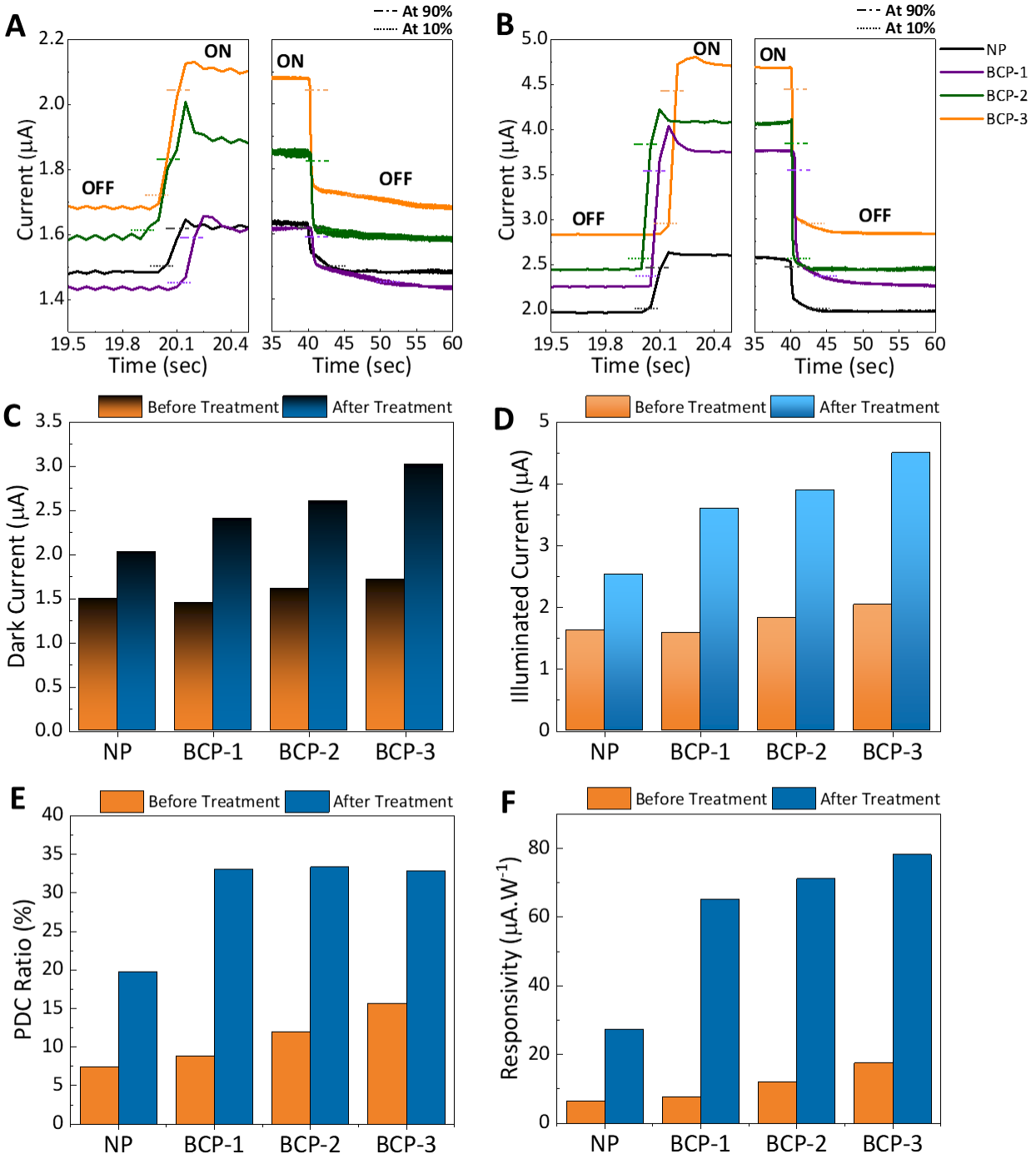

Figure S32. Photoelectrochemical response of CuTe for NP, BCP-1, BCP-2, and BCP-3 films. Current transients observed at the response and recovery on films (A) before and (B) after treatment. (C) Dark current, (D) illuminated current, (E) photo-to-dark current (PDC) ratio, and (F) responsivity of CuTe before and after treatment.

Supporting Information Note 7

Photoelectrochemical response

The transient response of the CuTe films showed improved performance upon exposure to optimal Ar plasma, with faster transient behavior and improvement in dark and illuminated currents. The observed values for plasma treated films are shown in Table S6. To understand the improvement in the films, the photo-to-dark current (PDC) ratio and responsivity of the films were compared before and after treatment (Figures S32E and S32F). The expression for the PDC ratio is given as

$$\%PDC = \frac{(I_i - I_d)}{I_d} \times 100$$

where I_i and I_d are the illuminated and dark currents, respectively, from the photocurrent $I_{ph} = I_i - I_d$. We observed a 71.14% improvement in films after exposure to plasma treatment, a 50.2% increase in the PDC ratio was observed in mesoporous films when compared to plasma treated NP films. Similarly, considering the performance with respect to the active area (A) and optical power input (P_{in}) to the film through photoelectrochemical analysis, the responsivity (R) of the film can be calculated by the equation

$$R = \frac{I_{Ph}}{A.P_{in}}$$

The responsivity of the plasma treated films was 83% higher than that of the pristine CuTe films (*i.e.*, untreated mesoporous CuTe films). Mesoporous films with larger surface areas and domain sizes showed 61% on average over the NP films. The extracted values are presented in Table S7. The observed results showed an improvement of orders of magnitude when compared to the untreated films. In addition, the mesoporous films could use their larger reactive surface area for photoconversion and enable carrier transport through nanoscale walls more efficiently by effectively managing the incoming photons, compared to the NP film in an aqueous electrolyte medium. The Ar plasma treatment at optimal conditions on the films enhanced the material properties significantly, and long-range ordered crystal structures with reduced surface states led to improved electrical performance. Overall, the BCP-3 film, with larger pore size and a much larger domain size owing to its thicker walls, as well as relatively lower Urbach energy value after plasma exposure, showed better performance than the BCP-1 and BCP-2 films.

Table S1. Energy levels of nonporous and mesoporous CuTe films observed by spectrophotometry and UPS analysis.

Sample Name	Treatment	Bandgap (E_g) (eV)	Urbach Energy (E_U) (eV)	Valence Band (VB) (eV)	Work-function (ϕ) (eV)
NP film	**Pristine**	2.41	0.599	5.97	3.90
	140 °C	2.24	0.438	6.29	4.25
	30 W	2.23	0.224	6.16	4.08
BCP-1 film	**Pristine**	2.50	0.900	6.78	4.71
	140 °C	2.33	0.466	6.72	4.61
	30 W	2.45	0.287	6.60	4.54
BCP-2 film	**Pristine**	2.36	0.842	6.30	4.26
	140 °C	2.34	0.412	6.21	4.16
	30 W	2.37	0.196	6.35	4.30
BCP-3 film	**Pristine**	2.28	0.713	6.33	4.26
	140 °C	2.26	0.358	6.39	4.35
	30 W	2.18	0.107	6.23	4.18

Table S2. The change of film thicknesses before and after plasma treatment at different power.

Sample Name	Film Thickness (nm)			
	Pristine	**30 W for 180 s**	**50 W for 180 s**	**60 W for 180 s**
NP film	150.3	150.0	146.6	124.2
BCP-1 film	234.1	233.8	226.7	189.2
BCP-2 film	221.1	221.0	214.6	186.9
BCP-3 film	214.4	214.2	209.6	181.1

Table S3. Crystallinity (%) of samples upon increasing plasma exposure duration at 30 W.

After Treated Sample	Exposure Duration (s)	Crystallinity (%)
NP film	180	73.39
BCP-1 film	180	74.24
BCP-2 film	180	63.69
BCP-3 film	60	52.12
	180	84.97
	240	83.38
	300	88.67

Table S4. *d*-spacing extracted from GIXD data of films after plasma treatment at 30 W for 180 s and BCP-3 film upon increasing plasma exposure duration.

(hkl)	NP film		BCP-1 film		BCP-2 film		BCP-3 film	
	2*θ* (˚)	***d* (Å)**	**2*θ* (˚)**	***d* (Å)**	**2*θ* (˚)**	***d* (Å)**	**2θ (˚)**	***d* (Å)**
(001)	12.7	6.96	12.7	6.96	12.7	6.97	12.7	6.98
(011)	25.2	3.53	25.2	3.53	25.2	3.53	25.2	3.52
(101)	31.1	2.87	31.1	2.87	31.1	2.88	31.1	2.87
(110)	35.9	2.50	35.9	2.50	35.9	2.50	35.9	2.50
(111)	38.3	2.35	38.3	2.35	38.2	2.35	38.3	2.35
BCP-3 film (hkl)	**60 s**		**180 s**		**240 s**		**300 s**	
	2*θ* (˚)	***d* (Å)**	**2*θ* (˚)**	***d* (Å)**	**2*θ* (˚)**	***d* (Å)**	**2*θ* (˚)**	***d* (Å)**
(001)	12.6	7.01	12.7	6.98	12.7	6.98	12.6	7.05
(011)	25.3	3.51	25.3	3.52	25.2	3.53	25.2	3.54
(101)	31.2	2.87	31.1	2.87	31.1	2.87	31.0	2.88
(110)	36.1	2.49	35.9	2.50	35.9	2.49	35.8	2.51
(111)	38.5	2.34	38.3	2.35	38.3	2.35	38.5	2.34

Table S5. Atomic percentage change in surface oxidation levels.

Sample Name	Treatment	As Deposited		After Aging	
		$CuO/Cu(OH)_2$ (at 934.6 eV)	**TeO_2 (at 576.07 eV)**	**$CuO/Cu(OH)_2$ (at 934.6 eV)**	**TeO_2 (at 576.07 eV)**
Nonporous film	**Pristine**	19.01	20.35	19.92	28.61
	140 °C	17.08	26.78	18.57	35.03
	30 W	11.56	12.52	8.340	16.04
BCP-1 film	**Pristine**	18.84	30.67	20.33	31.48
	140 °C	26.10	29.12	36.04	36.15
	30 W	8.240	16.19	9.110	18.41
BCP-2 film	**Pristine**	19.07	27.87	32.48	35.16
	140 °C	25.12	28.89	29.32	33.96
	30 W	8.750	13.70	12.79	18.60
BCP-3 film	**Pristine**	16.51	27.29	20.41	31.19
	140 °C	18.57	28.83	19.47	39.30
	30 W	10.14	13.48	13.22	19.43

Note: We utilized only the TeO_2 peaks to calculate the surface oxidation level because trace amounts of other Te suboxide layers such as $Te(II)O/Te(II)(OH)_2$ were negligible.

Table S6. Photoelectrochemical behavior of CuTe before and after 30 W plasma treatment.

Sample Name	Before Treatment (Pristine)				After Treatment (30 W Plasma)			
	Response Time (s) $R_{1(BT)}$	**Recovery Time (s) $R_{2(BT)}$**	**OFF Current (μA) $I_{D(BT)}$**	**ON Current (μA) $I_{I(BT)}$**	**Response Time (s) $R_{1(AT)}$**	**Recovery Time (s) $R_{2(AT)}$**	**OFF Current (μA) $I_{D(AT)}$**	**ON Current (μA) $I_{I(AT)}$**
NP film	0.0889	2.67	1.50	1.62	0.0752	2.19	2.03	2.53
BCP-1 film	0.0762	10.4	1.45	1.59	0.0383	2.52	2.41	3.60
BCP-2 film	0.134	1.77	1.61	1.83	0.0401	0.182	2.60	3.90
BCP-3 film	0.104	5.81	1.72	2.04	0.0410	0.502	3.02	4.50

Note: All the values in Table S6 were extracted at 10% and 90% of the observed photoelectrochemical response.

Table S7. PDC ratio (%) and responsivity of CuTe before and after 30 W plasma treatment.

Sample Name	Before Treatment (Pristine)		After Treatment (30 W Plasma)	
	PDC Ratio (%)	**Responsivity, R ($\mu A\ W^{-1}$)**	**PDC Ratio (%)**	**Responsivity, R ($\mu A\ W^{-1}$)**
NP film	8.00	6.57	24.6	27.4
BCP-1 film	9.70	7.66	49.4	65.1
BCP-2 film	13.7	12.0	50.0	71.2
BCP-3 film	18.6	17.5	49.0	78.3

Note: All the values in Table S7 were extracted at 10% and 90% of the observed photoelectrochemical response.

References

[1] H. B. Michaelson, *J. Appl. Phys.* **1977**, *48*, 4729-4733.

[2] M. C. Biesinger, *Surf. Interface Anal.* **2017**, *49*, 1325-1334.

[3] Z. Wu, Y. Zhang, Y. Shen, W. Zhang, G. Shao, *Adv. Mater. Interfaces* **2020**, *7*, 2000854.

[4] S. Das, J. Appenzeller, *Nano Lett.* **2013**, *13*, 3396-3402.